Topology optimization applied to the design of Tesla-type turbine devices

Diego Hayashi Alonso[a], Emílio Carlos Nelli Silva[a,*]

[a]*Department of Mechatronics and Mechanical Systems Engineering, Polytechnic School of the University of São Paulo, Av. Prof. Mello Moraes, 2231, 05508-030, SP, Brazil*

Abstract

Tesla-type turbine devices are turbine devices which convert fluid motion into the rotating motion of a rotor, but without the need of any blades. This is possible due to the interaction of the boundary layer with the rotating fluid motion. In order to successfully optimize this type of fluid flow device through the topology optimization method, some relevant aspects need to be considered. The first one is due to its unique configuration, meaning that the 2D swirl flow model may be considered, which is much less computationally expensive than considering a "full" 3D model. Moreover, since higher mesh resolutions may be necessary in the design of Tesla-type turbines from to the possible appearence of smaller disk-like structures, this may increase the overall optimization cost if the traditional Taylor-Hood elements (quadratic finite elements for the velocity) are considered. This additional computational cost may be reduced by considering MINI elements (linear finite elements with bubble enrichment for the velocity) instead. Another modification that may be useful in its design is augmenting the traditional Brinkman model used in topology optimization with an additional inertial term (Brinkman-Forchheimer model), which may lead to better optimized Tesla turbine designs. Another factor to be considered is the multi-objective function, which may be defined to minimize the relative energy dissipation and maximize the power transferred from the fluid. In such case, the power objective function may be augmented with an additional porosity (material model) term. Numerical examples are presented, taking into account some aspects of the design of Tesla-type turbine devices.

Keywords: Topology optimization, 2D swirl flow, Brinkman-Forchheimer model, Finite element method, MINI elements, Tesla turbine

1. Introduction

The performance of fluid flow devices is an important factor in the design of fluid flow systems, such as valves, nozzles, channels, pumps and turbines. Turbines are fluid devices aimed at converting a given fluid motion into the rotating motion of a rotor, which, in turn, is used, for example, for energy generation. There are various possible designs for such devices, such as screw, Pelton, axial, and centrifugal bladed turbines, which rely on the variation of the linear momentum of the fluid induced by the blades. There is a specific type of fluid device that does not rely on blades in order to induce the movement of the rotor: the rotating fluid from the inlet drags the rotor by relying on the boundary layer effect. In this text, for simplicity, this basic principle (fluid drag effect due to the boundary layer) is referred to as "*Tesla principle*". Thus, some different designs may arise, such as Tesla [1], tubular adhesion [2], filamentous [3] and spiral [4] turbines. Among these various different designs, the designs that rely solely on the dragging effect of the boundary layer (i.e., not relying on structures (such as blades) to drag (or help dragging) the fluid) can be referred to as "Tesla-type fluid flow devices". The basic form of these devices consists of axisymmetric geometries, which can be given, essentially, by the basic forms of the Tesla turbine, which is composed of parallel rotating disks, as shown in Fig. 1, and the tubular adhesion turbine, which is composed of concentric rotating cylinders, as shown in Fig. 2.

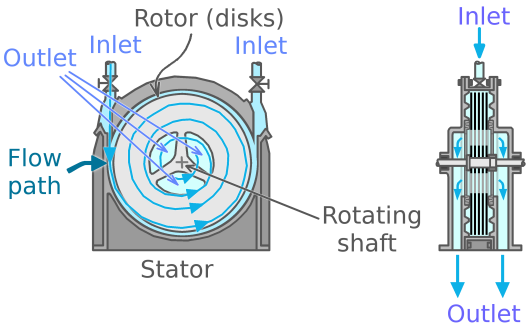

Figure 1: Tesla turbine according to Tesla's original patent (based on Tesla [1])

*Corresponding author. Tel.: +55 11 3091 9754; fax: +55 11 3091 5722.

Email address: ecnsilva@usp.br (Emílio Carlos Nelli Silva)

Published article (Published in its final form: March, 2022):
Alonso, D.H. & Silva, E.C.N. **Topology optimization applied to the design of Tesla-type turbine devices**. Applied Mathematical Modelling 103, 764–791 (2022).
https://doi.org/10.1016/j.apm.2021.11.007

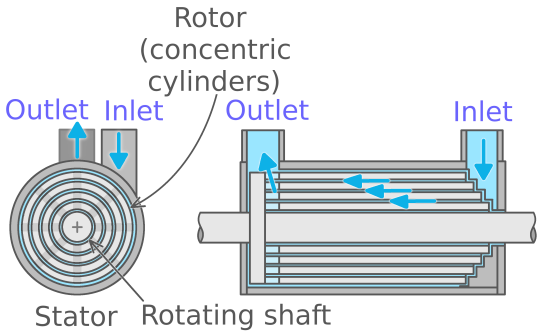

Figure 2: Tubular adhesion turbine (based on Ford [2])

The Tesla turbine can be perceived as an almost pure impulse turbine, portraying a large pressure drop in the nozzle while having a small pressure drop in the rotor [5]. Some advantages of Tesla turbines in comparison to bladed turbines are [6, 7]: lower cost (i.e., simpler manufacturing, maintenance and balancing), lower noise (which means less vibration), higher safety under higher rotations (since there are no blades with risk of breakage under excessively high rotations), self-cleaning nature (due the centrifugal effect), and independence from the direction of the rotation. Another relevant aspect is the capacity to operate under a large variety of fluids, such as Newtonian, non-Newtonian, mixtures, mixed with particulates (such as from biomass), steam, gases etc [8, 9, 10, 11, 12, 13, 6, 7]. According to Rey Ladino [7], one problem of the Tesla turbine is the low efficiency, which is in the range of 10% to 50%.

In this work, the topology optimization method is used to design Tesla-type turbine devices. The topology optimization method is based on the optimization of the distribution of a given design variable (i.e., the solid/fluid material) over a design domain. It was first introduced in fluid problems by Borrvall and Petersson [14] ("pseudo-density approach"). Other approaches have also arisen, such as by using the "level-set method" [15, 16, 17], or topological derivatives [18, 19]. In this work, the "pseudo-density approach" is used. A wide variety of flow types has already been considered in topology optimization: Stokes flows [14], Navier-Stokes flows [20, 21], slightly compressible flows [22], compressible flows [23], Darcy-Stokes flows [24, 25], non-Newtonian flows [26, 27], thermal-fluid flows [28, 29, 30], turbulent flows [31, 32, 33], unsteady flows [34, 35] etc. Some fluid devices that have already been designed through topology optimization are valves [36, 37], rectifiers [38], mixers [39, 40], and flow machine rotors [41, 42, 43].

In a Tesla-type turbine device, the fluid flow may be modeled by assuming that the fluid rotates axisymmetricaly around an axis. Particularly, the 2D swirl flow model shows good agreement with experiments and 3D simulations [7, 44, 45]. However, it may neglect some inlet/outlet geometries, some specific flow oscillations [44] and the presence of auxiliary non-axisymmetric structures needed for the mechanical assembly of the fluid flow device. Some of these structures that are necessary for the fabrication are circumferentially spaced spacers/pins [46, 47] or arms connecting to the central shaft [1, 48, 49] (see Fig. 3). These additional structures should pose a small change in the fluid flow, which can be measured by the "blockage ratio" described in Dodsworth [50]. Also, in a Tesla turbine design, in order to achieve a rotating inlet velocity, some common approaches are, for example, considering one or more tubes directed at a circular volute [1, 51, 52, 7, 48], or a single inlet split into a "cylindrical flow" [45]. Some examples of fluid flow devices that can be modeled by the 2D swirl flow model are hydrocyclones [44, 53, 54, 55], swirling nozzles/diffusers [56, 57, 58], some labyrinth seals [59, 60] and some pumps and turbines [61, 1, 2]. This means that a 2D swirl flow model [62, 63] may be used for modeling a Tesla turbine rotor. In comparison to a complete 3D model, the main advantage of this model is the lower computational cost.

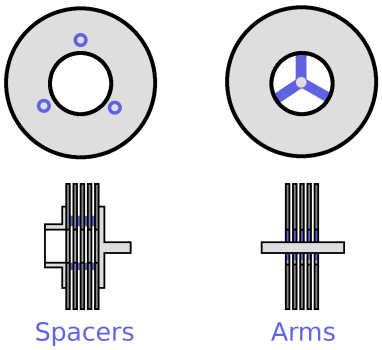

Figure 3: Examples of some of the possible configurations of "spacers" and "arms" being used to attach disk structures in a traditional Tesla turbine case. It is also possible to combine both ("spacers" and "arms") simultaneously

Therefore, the main objective of this work is to design Tesla-type turbine devices (such as the ones given by the basic forms of Figs. 1 and 2) by using the topology optimization method based on a 2D swirl flow model. The modeling is performed through the finite element method. The material model of fluid topology optimization [14] is extended by including not only the Darcy term [64] (which corresponds to a "permeability effect" and is the model that has been frequently used in fluid topology optimization), but also the Forchheimer term (which corresponds to an "inertia effect") [65]. This inclusion is shown in this work to possibly lead to better optimized Tesla-type turbine designs. This type of augmentation in the material model is called "Brinkman-Forchheimer model", and has been previously applied by Philippi and Jin [66] in topology optimization to model solid material, being referred there as the "complete porosity formulation". The formulation presented by Philippi and Jin [66] does not directly match the topology optimization formulation first presented by Borrvall and Petersson [14], therefore it is

reformulated in this work. The design variable is considered to be nodal. A multi-objective function is defined to minimize energy dissipation and maximize the power transferred from the fluid. The power objective function is augmented with a porosity (material model) term, which better matches the energy dissipation definition from Borrvall and Petersson [14]. The fluid is considered to be incompressible, with the properties of air at 25°C. Since higher mesh resolutions may be necessary in the design of Tesla-type turbines due to smaller disk-like structures appearing, the computational cost from using the traditional Taylor-Hood elements (quadratic velocity interpolation) increases the overall optimization cost. In order to reduce the computational cost, MINI elements [67] (linear interpolation with bubble enrichment for the velocity) are used.

This paper is organized as follows: in Section 2, the fluid flow model is described for 2D swirl flow; in Section 3, the weak formulation of the problem and the finite element modeling are presented; in Section 4, the topology optimization problem is stated by considering the Brinkman-Forchheimer model; in Section 5, the numerical implementation is briefly described; in Section 6, numerical examples are presented; and in Section 7, some conclusions are inferred.

2. Equilibrium equations

The fluid flow modeling is performed for low Reynolds number configurations, incompressible fluid and steady-state regime, by solving the equations for continuity and linear momentum (Navier-Stokes).

2.1. 2D swirl flow model

The differential equations for fluid flow are given under a rotating reference frame as [68, 69, 41]

$$\nabla \bullet \boldsymbol{v} = 0 \tag{1}$$

$$\rho \nabla \boldsymbol{v} \bullet \boldsymbol{v} = \nabla \bullet \boldsymbol{T} + \rho \boldsymbol{f} - 2\rho(\boldsymbol{\omega} \wedge \boldsymbol{v}) - \rho \boldsymbol{\omega} \wedge (\boldsymbol{\omega} \wedge \boldsymbol{r}) + \boldsymbol{f}_r(\alpha) \tag{2}$$

where $\boldsymbol{v}$ is the fluid velocity in relation to the rotating reference frame, p is the fluid pressure, ρ is the fluid density, μ is the fluid dynamic viscosity, $\rho \boldsymbol{f}$ is the body force per unit volume acting on the fluid, $\boldsymbol{r}$ is radial position with respect to the rotation axis (in 2D swirl flow, it is equivalent to use $\boldsymbol{s}$ (position)), $\wedge$ is used to denote cross product, $-2\rho(\boldsymbol{\omega} \wedge \boldsymbol{v})$ is the Coriolis force, $-\rho \boldsymbol{\omega} \wedge (\boldsymbol{\omega} \wedge \boldsymbol{r})$ is the centrifugal inertial force, $\boldsymbol{f}_r(\alpha)$ is the resistance force of the porous medium used in topology optimization, α is the pseudo-density, which may attain values that range from 0 (solid) to 1 (fluid) (and is also considered as the design variable in topology optimization), and $\boldsymbol{T}$ is the stress tensor given by

$$\boldsymbol{T} = 2\mu \boldsymbol{\epsilon} - p\boldsymbol{I} \ , \ \boldsymbol{\epsilon} = \tfrac{1}{2}(\nabla \boldsymbol{v} + \nabla \boldsymbol{v}^T) \tag{3}$$

The 2D swirl flow model, which can also be referred as "2D axisymmetric model with swirl", considers axisymmetry and cylindrical coordinates (as shown in Fig. 4). In such case, the position and velocity become

$$\boldsymbol{r} = (r,\ 0,\ z) = r\boldsymbol{e}_r + z\boldsymbol{e}_z \tag{4}$$

$$\boldsymbol{v} = (v_r,\ v_\theta,\ v_z) = v_r\boldsymbol{e}_r + v_\theta\boldsymbol{e}_\theta + v_z\boldsymbol{e}_z \tag{5}$$

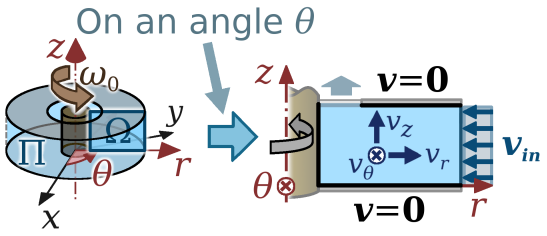

Figure 4: Representation of the 2D swirl flow model exemplified for a Tesla-type turbine device.

From axisymmetry, the derivatives of the state variables ($\boldsymbol{v}$ and p) in the θ direction are zero (i.e., $\frac{\partial v_r}{\partial \theta} = \frac{\partial v_\theta}{\partial \theta} = \frac{\partial v_z}{\partial \theta} = \frac{\partial p}{\partial \theta} = 0$). The equations for the 2D swirl flow model are further developed in Alonso et al. [62].

2.2. Boundary value problem

Generically, the boundaries for the computational domain when considering a 2D swirl flow model may include the symmetry axis or not, which is shown in Fig. 5. Then, the boundary value problem for the 2D swirl flow model can be stated as follows [62, 63].

$$\begin{aligned}
\rho \nabla \boldsymbol{v} \bullet \boldsymbol{v} = \nabla \bullet \boldsymbol{T} + \rho \boldsymbol{f} - 2\rho(\boldsymbol{\omega} \wedge \boldsymbol{v}) - & \\
\rho \boldsymbol{\omega} \wedge (\boldsymbol{\omega} \wedge \boldsymbol{r}) + \boldsymbol{f}_r(\alpha) & \quad \text{in } \Omega \\
\nabla \bullet \boldsymbol{v} = 0 & \quad \text{in } \Omega \\
\boldsymbol{v} = \boldsymbol{v}_{in} = (v_{r,in},\ 0,\ 0) & \quad \text{on } \Gamma_{\text{in}} \\
\boldsymbol{v} = \boldsymbol{0} & \quad \text{on } \Gamma_{\text{wall}} \\
v_r = 0 \text{ and } \frac{\partial v_r}{\partial r} = \frac{\partial v_\theta}{\partial r} = \frac{\partial v_z}{\partial r} = \frac{\partial p}{\partial r} = 0 & \quad \text{on } \Gamma_{\text{sym}} \\
\boldsymbol{T} \bullet \boldsymbol{n} = \boldsymbol{0} & \quad \text{on } \Gamma_{\text{out}}
\end{aligned} \tag{6}$$

where Ω, Γ_{in}, Γ_{wall}, Γ_{sym} and Γ_{out} can be visualized in Fig. 5. The inlet boundary (Γ_{in}) consists of a rotating inlet under the same rotation as the reference frame (ω_0). On the walls (Γ_{wall}), the no-slip condition is imposed. If there is a symmetry axis (Γ_{sym}) bordering the computational domain, the derivatives in relation to the r coordinate are considered to be zero, as well as the radial velocity. The outlet boundary (Γ_{out}) consists of a stress free condition

(i.e., open to the atmosphere), where $\boldsymbol{n}$ is the normal vector to the boundaries (pointing outside).

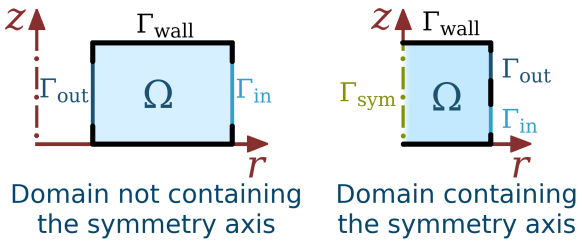

Figure 5: Boundaries that can be considered for 2D swirl flow devices.

3. Finite element method

The finite element method is solved through the weak formulation and finite elements described as follows.

3.1. Weak formulation

In the finite element method, the equilibrium equations of 2D swirl flow are modeled by a corresponding weak form. By considering the weighted-residual and Galerkin methods for the mixed (velocity-pressure) formulation, [70, 62]

$$R_c = \int_\Omega [\nabla \bullet \boldsymbol{v}] w_p r d\Omega \tag{7}$$

$$\begin{aligned} R_m = & \int_\Omega [\rho \nabla \boldsymbol{v} \bullet \boldsymbol{v} - \rho \boldsymbol{f} + 2\rho(\boldsymbol{\omega} \wedge \boldsymbol{v}) \\ & + \rho \boldsymbol{\omega} \wedge (\boldsymbol{\omega} \wedge \boldsymbol{r})] \bullet \boldsymbol{w}_v r d\Omega + \int_\Omega \boldsymbol{T} \bullet (\nabla \boldsymbol{w}_v) r d\Omega \\ & - \oint_\Gamma (\boldsymbol{T} \bullet \boldsymbol{w}_v) \bullet \boldsymbol{n} r d\Gamma - \int_\Omega \boldsymbol{f}_r(\alpha) \bullet \boldsymbol{w}_v r d\Omega \end{aligned} \tag{8}$$

where the subscripts c and m refer to the "continuity" and the "linear momentum" (Navier-Stokes) equations, respectively. The test functions of the state variables (p and $\boldsymbol{v}$) are given by w_p and $\boldsymbol{w}_v = \begin{bmatrix} w_{v,r} \\ w_{v,\theta} \\ w_{v,z} \end{bmatrix}$, respectively. Since the integration domain ($2\pi r d\Omega$) has a constant multiplier (2π), which does not influence when solving the weak form, eqs. (7) and (8) are given divided by 2π [62, 63].

From the mutual independence of the two test functions (w_p and $\boldsymbol{w}_v$), the equations of the weak form (eqs. (7) and (8)) can be summed to a single equation

$$F = R_c + R_m = 0 \tag{9}$$

3.2. Finite element modeling

In order to avoid instabilities and non-physical oscillations in the pressure [71], a finite element which obeys the LBB (Ladyžhenskaya-Babuška-Brezzi) condition [72, 73, 74] is normally chosen. The most commonly chosen finite element is the Taylor-Hood element, whose lowest degree version is given by using a linear interpolation for pressure (P_1 element) and a quadratic interpolation for velocity (P_2 element). Due to this quadratic interpolation, Taylor-Hood elements can be quite computationally demanding. In order to be able to use a linear interpolation for the velocity, which is computationally less expensive than the quadratic interpolation, while maintaining the finite element stable, stabilization methods have been proposed, such as pressure [75, 76, 77] and SUPG [78] stabilizations. One problem of these methods is that they include stabilization parameters which may have to be calibrated for the problem that is being solved. A way of using a lower interpolation for the velocity without relying on stabilization parameters is by enriching the linear element (P_1) with bubble shape functions (B_3) [67, 75]. In this case, the elements are called "MINI" and have been proven to be LBB stable by Arnold et al. [67]. The finite elements are represented in Fig. 6. A linear (nodal) interpolation (P_1 element) is used for the pseudo-density (design variable).

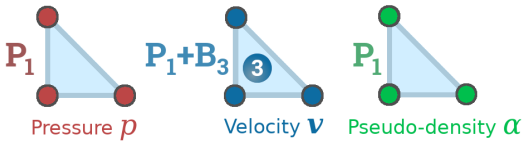

Figure 6: Finite elements chosen for the pressure-velocity formulation (MINI elements) and the design variable (pseudo-density).

4. Formulation of the Topology optimization problem

4.1. Material model

The material model of fluid topology optimization [14] is extended in order to include not only the Darcy term [64] ("Brinkman model") of the original formulation, but also the Forchheimer term [65]. This type of augmentation in the material model has been previously applied by Philippi and Jin [66] in topology optimization to model solid material, and is referred to as the "complete porosity formulation". In relation to the name "Brinkman model" [79], which refers to the case where only the Darcy term is considered, some references refer to the model including the Forchheimer term as the "Brinkman-Forchheimer model" (or "Forchheimer model") [80, 81]. In order to match the topology optimization formulation presented first by Borrvall and Petersson [14], the Brinkman-Forchheimer model is briefly derived and formulated as shown in the following Section.

4.1.1. Brinkman-Forchheimer model

According to Geertsma [82], when modeling a porous medium, the Darcy's law (linear law) is only valid to model porous material when the velocity is low (sufficiently

low Reynolds numbers) [83] and when the flow is single-phase [84, 64, 85]. The more generic equation is given by the Forchheimer's law (quadratic law), including the Forchheimer correction ("non-Darcy flow behavior") to the Darcy's law. The original formulation of Forchheimer's law is given by the pressure drop in a porous medium [65, 82, 86, 87, 88].

$$-\nabla p = \underbrace{\frac{\mu}{k_D}\boldsymbol{v}_{\text{mat}}}_{\text{Darcy term}} + \underbrace{\beta_F \rho |\boldsymbol{v}_{\text{mat}}| \boldsymbol{v}_{\text{mat}}}_{\text{Forchheimer term}} \tag{10}$$

where μ is the dynamic viscosity, ρ is the density, k_D is the formation permeability, p is the pressure, $\boldsymbol{v}_{\text{mat}}$ is the velocity in relation to the porous material ($\boldsymbol{v}_{\text{mat}} = (v_r,\ v_\theta - \omega_{\text{mat}} r,\ v_z)$, where ω_{mat} is the rotation of the porous medium in relation to the reference frame), β_F is the coefficient of inertial flow resistance, and $|\boldsymbol{v}_{\text{mat}}| = \sqrt{\boldsymbol{v}_{\text{mat}} \bullet \boldsymbol{v}_{\text{mat}}}$.

The influence of each term of eq. (10) is represented in Fig. 7: the Darcy term gives the reduction of the size of the fluid path due to the porous medium, while the Forchheimer term gives the fluid deceleration due to the inertia of the particles of the porous medium.

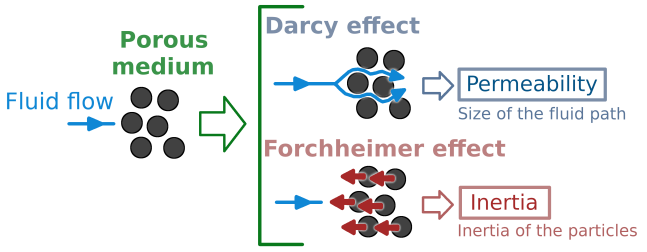

Figure 7: Darcy and Forchheimer effects in porous medium.

According to Cimolin and Discacciati [89], $\beta_F = \frac{C_F}{\sqrt{k_D}}$, where C_F is the dimensionless form-drag constant [86], also called Forchheimer constant [81]. Therefore, by representing the porous medium of eq. (10) as a resistance force of the porous medium ($\boldsymbol{f}_r(\alpha)$ of eq. (2)), and considering $\frac{\mu}{k_D} \equiv \kappa(\alpha)$ and $\frac{\rho}{\sqrt{\mu}} C_F \equiv k_{\text{inertia}}$

$$\boldsymbol{f}_r(\alpha) = \underbrace{-\kappa(\alpha)\boldsymbol{v}_{\text{mat}}}_{\text{Darcy term}} \underbrace{-k_{\text{inertia}}\sqrt{\kappa(\alpha)}|\boldsymbol{v}_{\text{mat}}|\boldsymbol{v}_{\text{mat}}}_{\text{Forchheimer term}} \tag{11}$$

where $k_{\text{inertia}} = \frac{\rho}{\sqrt{\mu}} C_F$ is the inertial resistance factor, and $\kappa(\alpha)$ is the inverse permeability ("absorption coefficient").

The Forchheimer constant C_F varies according to the type of porous medium [87, 90, 91]. If the diameter of the porous medium "particles" is much smaller than the microscopic scale [66], C_F can be assumed as a "universal" constant [92] given by $C_F = 0.55$ [66]. Since, in topology optimization, the porous material is used to model a solid wall and not a specific type of porous material, C_F is assumed as 0.55 in this work.

Eqs. (1) and (2) considering eq. (11) consist of a well-posed problem according to Varsakelis and Papalexandris [93]. The other approach for modeling the Forchheimer equation is given by the semi-empirical approach (Carman-Kozeny equation) [94, 95, 96], which includes dependency on microscopic and macroscopic particles characteristics of the porous medium, distancing the porosity modeling from the modeling of solid material used in this work.

4.1.2. Material model for the inverse permeability

Since the objective in topology optimization is to obtain a sufficiently discrete distribution of the design variable (pseudo-density) inside the design domain, the subtle transition between the binary values 0 (for solid) and 1 (for fluid) is "relaxed". This "relaxation" allows an intermediate porous medium (normally referred as a "gray" material, with a pseudo-density between 0 and 1 (real values)). Borrvall and Petersson [14] considers the following convex interpolation function for the inverse permeability:

$$\kappa(\alpha) = \kappa_{\max} + (\kappa_{\min} - \kappa_{\max})\alpha \frac{1+q}{\alpha+q} \tag{12}$$

where the value of the inverse permeability ($\kappa(\alpha)$) is bounded by a maximum value ($\kappa_{\max}$) and a minimum value ($\kappa_{\min}$), and has its convexity (relaxation) controlled by the penalization parameter $q > 0$ (large values of q lead to a less relaxed material model). It is also possible to optionally define $\kappa_{\max}$ in function of a dimensionless number (a maximum Darcy number, "$\text{Da}_{\max}$"), which is given as [21]:

$$\text{Da}_{\max} = \frac{\mu}{\kappa_{\max} L_{\text{ref}}^2} \tag{13}$$

where L_{ref} is a characteristic dimension of the computational domain, and may be given, for example, as $L_{\text{ref}} = 2r_{ext}$, where r_{ext} is the most external radius of the computational domain. Due to this work considering more than one computational domain in the numerical examples, for clarity, $\kappa_{\max}$ is expressed as $\frac{1}{\text{Da}_{\max} L_{\text{ref}}^2}$, by indicating its value in function of μ.

4.2. Topology optimization problem

The topology optimization problem can be formulated as follows.

$$\begin{aligned} &\min_{\alpha}\ J(p(\alpha), \boldsymbol{v}(\alpha), \alpha) \\ &\textbf{such that} \\ &\quad \text{Fluid volume constraint: } \int_{\Omega_\alpha} \alpha(2\pi r d\Omega_\alpha) \leqslant f V_0 \\ &\quad \text{Box constraint of } \alpha\text{: } 0 \leqslant \alpha \leqslant 1 \end{aligned} \tag{14}$$

where f is the specified volume fraction, $V_0 = \int_{\Omega_\alpha} 2\pi r d\Omega_\alpha$ is the volume of the design domain (represented as Ω_α), $J(p(\alpha), \boldsymbol{v}(\alpha), \alpha)$ is the objective/multi-objective function, and $p(\alpha)$ and $\boldsymbol{v}(\alpha)$ are the pressure and velocity obtained by solving the boundary value problem (eq. (6)), which features an indirect dependency with respect to the design variable α.

4.3. Energy dissipation

The relative energy dissipation is used as the objective function based on the energy dissipation defined in Borrvall and Petersson [14] and considering inertial effects, as defined in Alonso et al. [63] for a rotating reference frame. By assuming zero external body forces,

$$\begin{aligned}\Phi_{\text{rel}} = &\int_\Omega \left[\frac{1}{2}\mu(\nabla \boldsymbol{v} + \nabla \boldsymbol{v}^T)\bullet(\nabla \boldsymbol{v} + \nabla \boldsymbol{v}^T)\right] 2\pi r d\Omega \\ &- \int_\Omega \boldsymbol{f}_r(\alpha)\bullet\boldsymbol{v} 2\pi r d\Omega \\ &+ \int_\Omega (2\rho(\boldsymbol{\omega}\wedge\boldsymbol{v}) + \rho\boldsymbol{\omega}\wedge(\boldsymbol{\omega}\wedge\boldsymbol{r}))\bullet\boldsymbol{v} 2\pi r d\Omega\end{aligned} \tag{15}$$

It can be mentioned that, since the rotation vector is given by $\boldsymbol{\omega} = \omega_0 \boldsymbol{e}_z$ and by considering eq. (4), the Coriolis term $(2\rho(\boldsymbol{\omega}\wedge\boldsymbol{v})\bullet\boldsymbol{v})$ becomes zero.

Borrvall and Petersson [14] demonstrated for Stokes flow that minimizing energy dissipation is closely related to maximizing the pressure increment of the outlet in relation to the inlet. In the case of Navier-Stokes flow, the energy dissipation becomes closely related to the pressure head. This relationship is shown in Appendix A.

4.4. Power

The power transferred from the fluid (P'_f) is given as the power transferred to the fluid (P_f) with a negative sign ($P'_f = -P_f$). Since $P'_f > 0$ for turbine devices (i.e., power is transferred from the fluid), this value can be used to define a "turbine power" (* On the opposite side, P_f would be a "pump power"). The power transferred to the fluid is given from the angular momentum equation when including the resistance force of the porous medium. According to Munson et al. [68], the integral form of the angular momentum equation is given by:

$$\begin{aligned}\frac{\partial}{\partial t}\int_\Omega (\boldsymbol{r}\wedge\boldsymbol{v}_{\text{abs}})\rho 2\pi r d\Omega + \oint_\Gamma (\boldsymbol{r}\wedge\boldsymbol{v}_{\text{abs}})\rho\boldsymbol{v}_{\text{abs}}\bullet\boldsymbol{n} 2\pi r d\Gamma \\ = \boldsymbol{r}\wedge\boldsymbol{F}_{\text{ext}}|_\Omega\end{aligned} \tag{16}$$

where $\boldsymbol{v}_{\text{abs}} = \boldsymbol{v} + \boldsymbol{\omega}\wedge\boldsymbol{r}$ (absolute velocity) and $\boldsymbol{F}_{\text{ext}}$ is the external force acting on the fluid. In eq. (16), the right side of the equation is given by

$$\boldsymbol{r}\wedge\boldsymbol{F}_{\text{ext}}|_\Omega = \boldsymbol{T}_{\text{ext}} - \int_\Omega \boldsymbol{r}\wedge(\rho\boldsymbol{f}) 2\pi r d\Omega - \int_\Omega \boldsymbol{r}\wedge\boldsymbol{f}_r(\alpha) 2\pi r d\Omega \tag{17}$$

where $\boldsymbol{T}_{\text{ext}}$ is the torque. The resistance force of the porous medium ($\boldsymbol{f}_r(\alpha)$) is included in a similar way as the body forces $\rho\boldsymbol{f}$.

Therefore, by substituting eq. (17), in eq. (16), assuming steady-state flow and zero external body forces,

$$\begin{aligned}\boldsymbol{T}_{\text{ext}} = &\oint_\Gamma (\boldsymbol{r}\wedge\boldsymbol{v}_{\text{abs}})\rho\boldsymbol{v}_{\text{abs}}\bullet\boldsymbol{n} 2\pi r d\Gamma \\ &+ \int_\Omega \boldsymbol{r}\wedge\boldsymbol{f}_r(\alpha) 2\pi r d\Omega\end{aligned} \tag{18}$$

Since $P_f = \boldsymbol{\omega}\bullet\boldsymbol{T}_{\text{ext}}$, the power is given by

$$\begin{aligned}P_f = &\oint_\Gamma \boldsymbol{\omega}\bullet(\boldsymbol{r}\wedge\boldsymbol{v}_{\text{abs}})\rho\boldsymbol{v}_{\text{abs}}\bullet\boldsymbol{n} 2\pi r d\Gamma \\ &+ \int_\Omega \boldsymbol{\omega}\bullet[\boldsymbol{r}\wedge\boldsymbol{f}_r(\alpha)] 2\pi r d\Omega\end{aligned} \tag{19}$$

The above equation includes the resistance force of the porous medium, which has not been previously included in this formulation [41, 42]. This additional "resistance force" term is analogous to the material model term of the energy dissipation defined by Borrvall and Petersson [14] and also shown in eq. (15).

4.5. Multi-objective function

In order to consider two objective functions in the topology optimization problem, a multi-objective function weighting both equations into one may be defined. Since the measurement units and magnitudes of each of the objective functions can be different, the objective function magnitudes and sensitivities may significantly vary from one another. In order to reduce such possible disparity and possible predominance of one objective function over the other during the optimization iterations, the following multi-objective function is used, based on the initial ratio between the objective functions,

$$J = w_\Phi \Phi_{\text{rel}} + w_P \left(\frac{\Phi_{\text{rel},0}}{P_{f,0}}\right) P_f \tag{20}$$

$$\frac{dJ}{d\alpha} = w_\Phi \frac{d\Phi_{\text{rel}}}{d\alpha} + w_P \left(\frac{\Phi_{\text{rel},0}}{P_{f,0}}\right) \frac{dP_f}{d\alpha} \tag{21}$$

where $P_f = -P'_f$ is the power transferred to the fluid, the weights w_Φ and w_P are constants ($w_\Phi + w_P = 1$), and $\Phi_{\text{rel},0}$ and $P_{f,0}$ are the values of the objective functions before starting the IPOPT algorithm.

4.6. Sensitivity analysis

The sensitivity is given by the adjoint method as

$$\left(\frac{dJ}{d\alpha}\right)^* = \left(\frac{\partial J}{\partial \alpha}\right)^* - \left(\frac{\partial F}{\partial \alpha}\right)^* \boldsymbol{\lambda}_J \tag{22}$$

$$\left(\frac{\partial F}{\partial(\boldsymbol{v}, p)}\right)^* \boldsymbol{\lambda}_J = \left(\frac{\partial J}{\partial(\boldsymbol{v}, p)}\right)^* \text{(adjoint equation)} \tag{23}$$

where J is the objective/multi-objective function, the weak form is given by $F = 0$, " * " represents conjugate transpose, and $\boldsymbol{\lambda}_J$ is the adjoint variable (Lagrange multiplier of the weak form). This way, the matrix forms of the terms of eqs. (22) and (23) are computed and the solutions of the resulting matrix systems directly result in $\frac{dJ}{d\alpha}$. Particularly, in this work, the matrix forms are automatically derived in dolfin-adjoint (using FEniCS).

5. Numerical implementation of the optimization problem

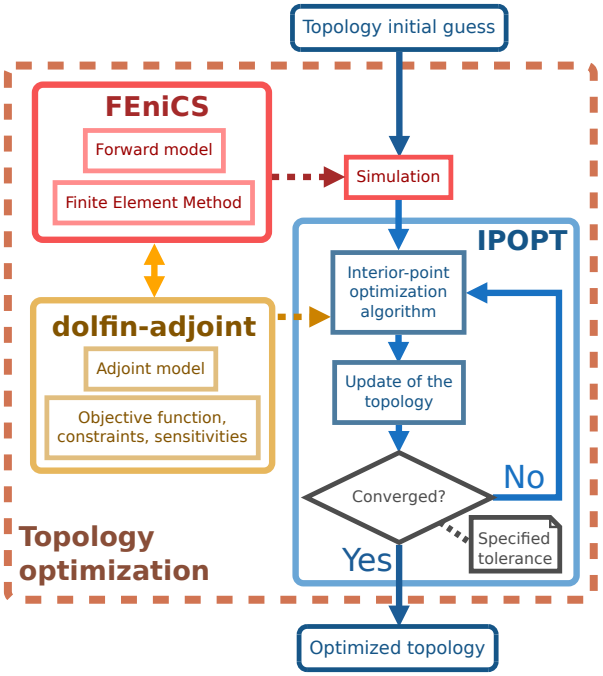

Figure 8: Flowchart representing the numerical implementation of the topology optimization problem.

The finite element method is computed by FEniCS platform [75], by using automatic differentiation and a high-level language (UFL) for representing the weak form and functionals for the finite element matrices. For the sensitivities of the topology optimization problem, the adjoint model is automatically obtained from the weak form and objective functions by the dolfin-adjoint library [97, 98]. IPOPT (Interior-Point Optimization algorithm) [99] is used as the algorithm for solving the topology optimization problem: Being an interior point method, it forces the solution to be searched in the feasible space, but also avoids having to compute the exact value of the penalty parameter of the logarithmic barrier at each iteration (by using a line-search filter method). The dolfin-adjoint library provides an interface for using it. The nonlinear weak form (eq. (9)) is solved by the Newton-Raphson method, in which the corresponding linearized problems at each iteration are solved with MUMPS (MUltifrontal Massively Parallel sparse direct Solver) [100].

The implementation of the topology optimization method is illustrated in Fig. 8. It starts with an initial guess for the distribution of the design variable (pseudo-density) in the design domain. Then, a simulation is performed with FEniCS from the finite element method and the forward model (i.e., the weak form and boundary conditions). This first simulation is used by dolfin-adjoint in order to obtain the adjoint model, which is then used in the optimization loop. The optimization loop is performed with IPOPT and continues until the specified tolerance (convergence criterion) is reached.

6. Numerical results

In the numerical results, the properties of the fluid being considered are of incompressible air at 25°C, with a dynamic viscosity (μ) of 18.37 $\times 10^{-6}$ Pa s [101], and a density (ρ) of 1.169 kg/m^3 [102].

The finite element meshes for all the numerical examples are structured and divided in rectangular partitions of 4 triangular elements each (see Fig. 9).

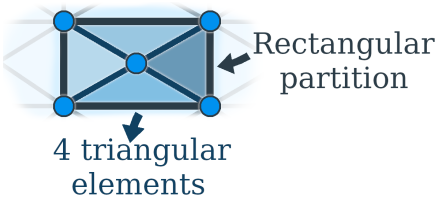

Figure 9: Triangular elements distributed in a rectangular partition of the mesh.

In order to achieve a better numerical conditioning for calculating the weak form, functionals and sensitivities, and also for improving the convergence rate, the MMGS (Millimeters-Grams-Seconds) unit system is used, which means that the length and mass units are multiplied by a 10^3 factor.

The Newton-Raphson method is computed with an absolute tolerance of 10^{-10}, and relative tolerance of 10^{-9}. The convergence criterion for the optimization is a tolerance of 10^{-10} for the optimality error of the IPOPT barrier problem, which is essentially the maximum norm of the KKT conditions [99].

The external body force term ($\rho \boldsymbol{f}$) is not considered for the numerical examples ($\rho \boldsymbol{f} = (0,\ 0,\ 0)$). The porous medium is considered to be rotating together with the reference frame ($\boldsymbol{v}_{\text{mat}} = \boldsymbol{v}$). The minimum value of the inverse permeability is assumed as zero ($\kappa_{\text{min}} = 0$ kg/(m^3 s)).

The initial guess for the design variable (pseudo-density) is the uniform distribution $\alpha = f - 1\%$, where f is the specified volume fraction and 1% is an assumed margin in order for the initial guess not to violate the volume constraint (because of the numerical accuracy of the calculations). The plots of the optimized topologies show the values of the design variable (α) in the center of each finite element. The letter n denotes rotation in rpm, and the greek letter ω denotes rotation in rad/s.

The values of the design variable (pseudo-density) in the optimized topologies are post-processed by a threshold (step) function:

$$\alpha_{\text{th}} = \begin{cases} 1 \text{ (fluid), if } \alpha \geqslant 0.5 \\ 0 \text{ (solid), if } \alpha < 0.5 \end{cases} \tag{24}$$

From the threshold function, a binary distribution is obtained for the design variable (α_{th}), which can then be cut in order to remove the solid material ($\alpha = 0$) from the computational domain (see Fig. 10). In such case, the final simulation can be performed with the Navier-Stokes equations without the effect of the porous medium (i.e., without the Brinkman/Brinkman-Forchheimer model). In this case, optimized topologies achieved with different optimization parameters can be compared. Except when highlighted otherwise, in all of the optimized topologies, the final values achieved for the design variable (pseudo-density) are close to the bounds (i.e., close to $\alpha = 0$ and $\alpha = 1$).

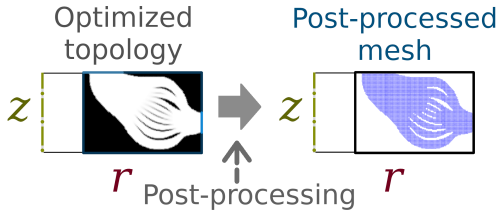

Figure 10: Illustration of the post-processing being applied for an optimized topology.

The pressure head can be calculated for the results from the integral form of the energy equation (1$^{\text{st}}$ Law of Thermodynamics) [68] by simplifying for an incompressible steady-state flow with negligible heat transfer. By also neglecting the effect of the height (i.e., the gravitational force),

$$H = \frac{1}{Q}\left[\oint_{\Gamma}\left(\frac{p}{\rho g} + \frac{{v_{\text{abs}}}^2}{2g}\right)\boldsymbol{v}_{\text{abs}} \bullet \boldsymbol{n} 2\pi r d\Gamma\right] \tag{25}$$

where Q is the flow rate. In turbine devices, it is expected that $H < 0$ (i.e., the fluid exits the turbine with less energy than when it enters) and $P_f < 0$ ($P'_f > 0$) (i.e., power is transferred from the fluid to the rotor). Therefore, in turbines, the opposite of the pressure head ($H' = -H$) is a positive value that can be used to define a "turbine pressure head" (* On the opposite side, H would be a "pump pressure head").

From the definitions of the pressure head (H, eq. (25)) and the power transferred to the fluid (P_f,eq. (19)), it is possible to define the isentropic efficiency for turbine devices as [102, 7]

$$\eta_s = \frac{P_{real}}{P_{ideal}} = \frac{P_f/\dot{m}}{\Delta h_s} = \frac{P_f/\dot{m}}{gH} \tag{26}$$

where $\dot{m}$ is the mass flow rate, and $\Delta h_s = gH$ is the variation of specific enthalpy (specific work) in the ideal process [102]. It can be mentioned that the fraction shown in eq. (26) is inverted for pumps (i.e., for pumps, $\eta_s = \frac{P_{ideal}}{P_{real}} = \frac{gH}{P_f/\dot{m}}$).

The Reynolds number can be calculated from the smallest size of the channels [7] or in function of the external radius. In this work, for simplicity, it is calculated as the maximum value of the local Reynolds number based on the external diameter:

$$\text{Re}_{\text{ext},\,\ell} = \frac{\mu\,|\boldsymbol{v}_{\text{abs}}|\,(2r_{ext})}{\rho} \tag{27}$$

where $\boldsymbol{v}_{\text{abs}}$ is the absolute velocity, which varies in each position of the computational domain, and r_{ext} is the most external radius of the computational domain.

In order to confirm that the air flow is still incompressible (Mach number smaller than 0.3 [69]), the Mach number may be calculated as the maximum value of the local Mach number:

$$\text{Ma}_{\ell} = \frac{|\boldsymbol{v}_{\text{abs}}|}{\sqrt{k_{\text{sh}}\frac{R_{\text{U}}}{M_{\text{molar}}}T_K}} \tag{28}$$

where $k_{\text{sh}} = \frac{c_p}{c_v} = 1.4$ (ratio of specific heats, where c_p considers a constant pressure, and c_v considers a constant volume) [102], $R_{\text{U}} = 8.31451$ J/(mol K) is the ideal gas constant, $M_{\text{molar}} = 28.96 \times 10^{-3}$ kg/mol is the molar mass of air [102] and $T_K = 298.15$ K (i.e., 25°C) is the temperature in Kelvin. In all numerical examples, the Mach number is smaller than 10^{-2}, which means that the fluid flow is incompressible.

6.1. Effect of the Brinkman-Forchheimer model

The first example is the design of a full-inlet turbine-type device by considering the Brinkman-Forchheimer model (as in the other examples) and the Brinkman model (i.e., eq. (11) without the Fochheimer term) (see Fig. 11): The computational domain is composed of a constant velocity inlet at the external radius r_{ext}, and the outlet is axial. The specified volume fraction (f) is 70%.

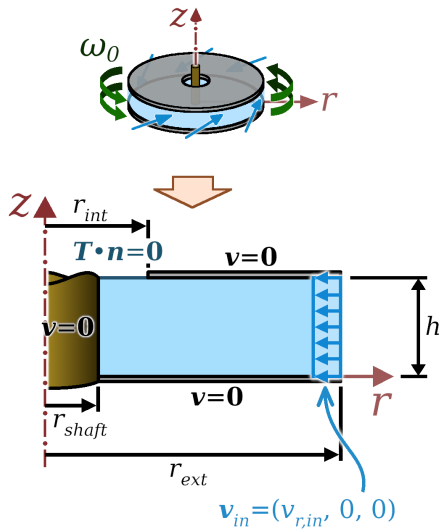

Figure 11: Design domain for the full-inlet turbine-type device.

Table 1: Parameters used for the topology optimization of the full-inlet turbine-type device.

Input parameters	
Inlet flow rate (Q)	2.0 L/min
Rotation	$n_0 = 1000$ rpm
Inlet rotation	$\omega_{in} = \omega_0$
Radial-axial inlet velocity profile	Constant
Dimensions	
h	5 mm
r_{shaft}	2.6 mm
r_{int}	5 mm
r_{ext}	10 mm

The finite element mesh is chosen with 132 radial and 60 axial rectangular partitions of crossed triangular elements, totaling 16,033 nodes and 31,680 elements (see Fig. 12). The input parameters and dimensions of the design domain that are used are shown in Table 1. The optimization scheme for this example is given by different values of $\kappa_{\max}$ considering $q = 10^3$. Among different values of $\kappa_{\max}$, the difference is essentially the "relaxation" of the strength of the material model, in which the fluid flow can be: insufficiently blocked, sufficiently blocked or "over" blocked. The case when "over" blocking of fluid flow occurs can hinder the topology optimization process, leading to an overly gray or simple/trivial local minima. When it is insufficiently blocked, sometimes a discrete topology may still be obtained, but it is also possible that the resulting topology be considered a worse local minima after post-processing.

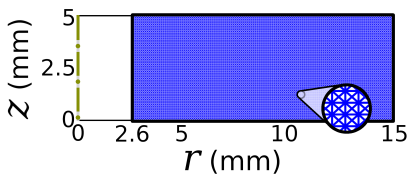

Figure 12: Mesh used for the full-inlet turbine-type device.

A series of optimizations is performed for a sequence of different values for $\kappa_{\max}$ for the Brinkman-Forchheimer and Brinkman models considering the relative energy dissipation as the objective function. Fig. 13 shows the objective function (relative energy dissipation) values with respect to $\kappa_{\max}$ for each optimized topology. The objective function values that are shown correspond to the post-processed mesh. The maximum value obtained for the maximum local Reynolds number ($\max(\mathrm{Re}_{\mathrm{ext},\,\ell})$) is 5.57 $\times$ 10^3. In fact, this value is below the transition Reynolds number in pumps (which is in the order of 10^6) [103, 104] and, since pumps can be said to represent the inverted operation of turbines, this means that the flow is most probably laminar.

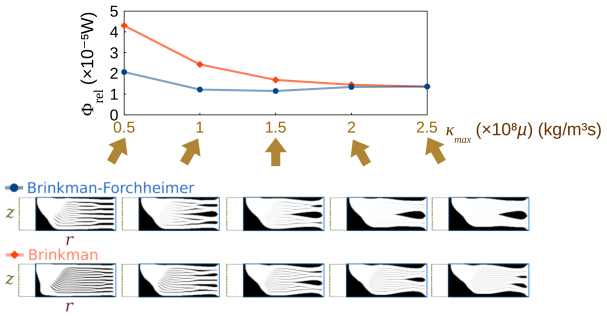

(a) Effect in the relative energy dissipation (Φ_{rel}).

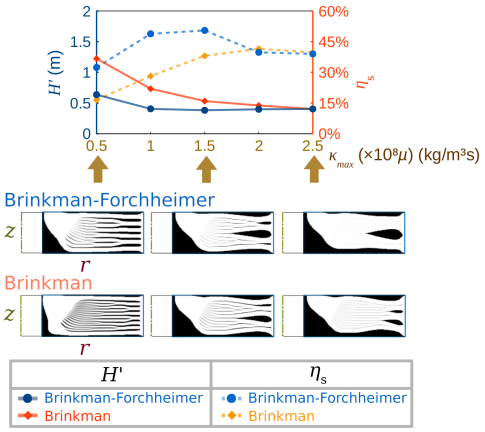

(b) Effect in the "turbine pressure head" ($H' = -H$) and isentropic efficiency (η_s).

Figure 13: Effect of $\kappa_{\max}$ in the design of the full-inlet turbine-type device for the Brinkman-Forchheimer and Brinkman models.

The optimized topologies are seen in Fig. 13a. As can be seen, the value of $\kappa_{\max}$ highly influences the quantity of fluid paths (i.e., disks) and their thickness and extension. The appearence of these intermediary "disk-like" structures reduces the dispersion of the fluid when entering the fluid flow device tending to lead to a more uniform effect of the "Tesla principle". When the material model is imposed with more "strength" (i.e., a higher $\kappa_{\max}$), this effect is diminished due to the fact that a small "gray" value in the pseudo-density (α) can now cause a greater disturbance in the fluid flow, which may induce a better or worse local minimum for the topology optimization problem. By comparing the topology optimization results by using the Brinkman model and the Brinkman-Forchheimer model, it can be noticed that the Brinkman-Forchheimer model led to optimized topologies with less relative energy dissipation than the Brinkman model, showing that, by using a more complete porosity formulation (Brinkman-Forchheimer model), a better local minima may be achieved. Fig. 13b shows a comparison of the values of the isentropic efficiency (η_s) and "turbine pressure head" (H'). In this case, it shows that the Brinkman-Forchheimer model attained mostly better isentropic efficiencies (η_s). However, the "turbine pressure head" (H') is slightly worse for the Brinkman-Forchheimer model. The reason for this difference is mainly due to the better spacing and size between the "disk-like" achieved by topology optimization.

It can also be highlighted that the objective functions are written differently for the Brinkman model and the Brinkman-Forchheimer model, since the Brinkman model includes only the Darcy term of $\boldsymbol{f}_r(\alpha)$ (eq. 11), whilst the Brinkman-Forchheimer model also includes the Forchheimer term. For the relative energy dissipation, the correspondance in the formulation of the objective function is shown in Appendix A, where the porous medium effect term as a whole is on the left-hand side of eq. (A.9).

The convergence curves for the full-inlet turbine-type devices follow similar patterns as the convergence curve shown in Fig. 22 for the two-inlet turbine-type device.

The simulation of the optimized topology for the full-inlet turbine-type device for $\kappa_{\max} = 1 \times 10^8 \mu$ (kg/(m^{3}s)) for the Brinkman-Forchheimer model is shown in Fig. 14.

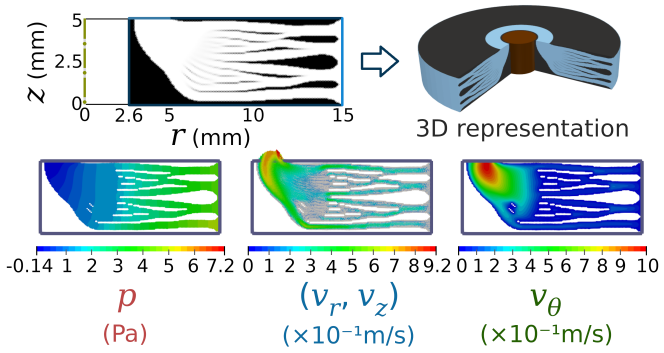

Figure 14: Optimized topology, 3D representation, pressure and velocity for the full-inlet turbine-type device for the Brinkman-Forchheimer model ($\kappa_{\max} = 1 \times 10^8 \mu$ (kg/(m^{3}s))).

Fig. 14 shows that the radial-axial flow ((v_r, v_z)) is separated into four paths and various following subpaths. The relative tangential velocity (v_θ) is consistent with this behavior, and accelerates near the outlet due to the effect of the "Tesla principle".

6.2. Effect of the power objective function

The second example is the design of a parallel-type turbine-type device by considering the multi-objective function for relative energy dissipation and power (see Fig. 15): The computational domain is composed of two parabolic inlets located at the external radius r_{ext}, and there are two outlets located at the internal radius r_{int}. It corresponds to the classical parallel channels ("double pipe") [14], but considered for 2D swirl flow in a turbine-type configuration (inlets at the external radius) and considering additional inlet and outlet channels. These additional channels serve as for not having any inlet/outlet to be partially blocked during topology optimization and are considered to be outside the design domain. The specified volume fraction (f) is 40%.

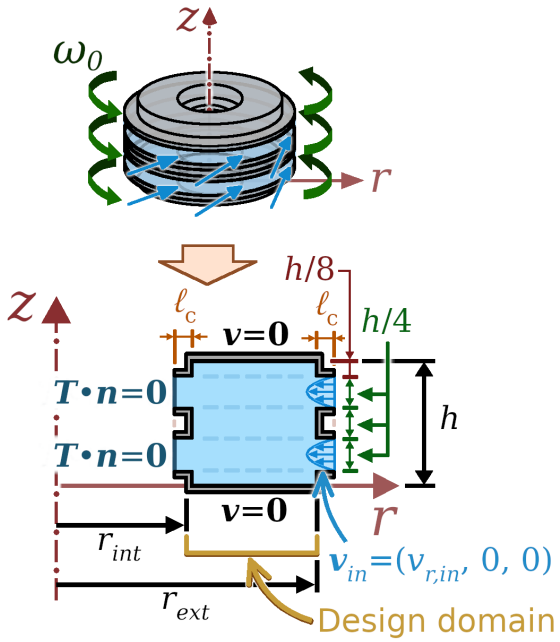

Figure 15: Design domain for the parallel-type turbine-type device.

The finite element mesh is composed of 7,823 nodes and 15,360 elements (see Fig. 16). The input parameters and dimensions of the design/computational domain that are used are shown in Table 2. The optimization scheme for this example is given by $\kappa_{\max} = 5 \times 10^8 \mu$ (kg/(m^{3}s)) and $q = 10^3$, without any special/specific treatment to avoid local minima (such as continuation in the topology optimization parameters and topology optimization filtering/projection). This is done in order to facilitate a comparison of the effect of the power objective function in topology optimization.

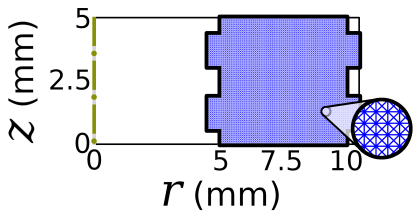

Figure 16: Mesh used for the parallel-type turbine-type device.

Table 2: Parameters used for the topology optimization of the parallel-type turbine-type device.

Input parameters	
Inlet flow rate (Q)	2.0 L/min
Rotation	$n_0 = 1000$ rpm
Inlet rotation	$\omega_{in} = \omega_0$
Radial-axial inlet velocity profile	Parabolic
Dimensions	
h	5 mm
ℓ_c	0.5 mm
r_{int}	5 mm
r_{ext}	10 mm

A series of optimizations is performed for a sequence of weights for the power transferred to the fluid (P_f) in the multi-objective function. In order to verify the effect in the optimized topology of the porosity term of the power objective function, the optimization is performed with and without the porosity term (with/without $\boldsymbol{f}_r(\alpha)$) shown in eq. (19). Fig. 17a shows the objective functions' values with respect to the weights of the objective functions for each optimized topology. The objective function values that are shown correspond to the post-processed mesh. Fig. 17b shows the corresponding isentropic efficiencies. The maximum value for the maximum local Reynolds number ($\max(\mathrm{Re}_{\mathrm{ext},\,\ell})$) is given as 2.99×10^3.

In Fig. 17, it can be noticed that the channels are straight until about $w_P = 0.6$ or $w_P = 0.8$, from which the optimized topologies start to significantly change. As can be noticed in the figure for the case including the porosity term, since both objective functions increased their values, it can be said that the corresponding optimized topologies should be local minima. When not including the porosity term, the effect of the power objective function seems to be "less aggressive" in the topology optimization than when including the porosity term, because the sensitivity of the energy dissipation predominates in the optimization due to its corresponding porosity term. The "gray" topologies $w_P = 1.0$ (indicated with an asterisk ("*")) indicate the optimized topologies that would result if only the power objective function is used, and the corresponding energy dissipation value is not represented due to the high presence of "gray" values for the design variable. As can be noticed, the power objective function alone is unable to create a fully discrete topology, and needs another function (such as the relative energy dissipation) in order to achieve the formation of fluid channels. By comparing these "gray" topologies, it can be noticed that, when including the porosity term in the objective function, this porosity term seems to contribute to the formation of channels, whereas not including it seems not to have such ten-

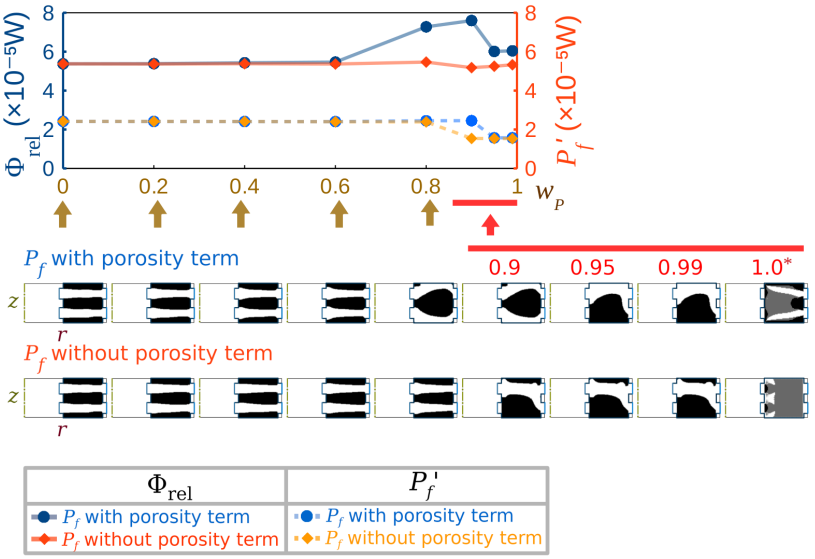

(a) Effect in the objective functions (Φ_{rel} and $P_f' = -P_f$).

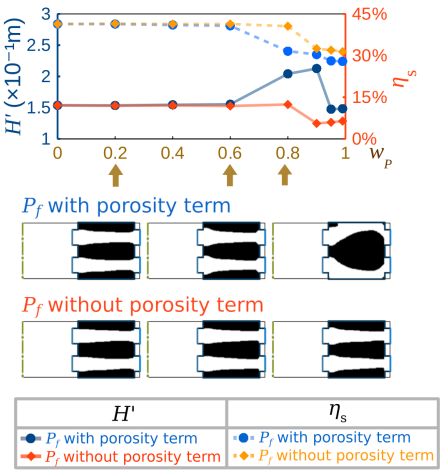

(b) Effect in the "turbine pressure head" ($H' = -H$) and isentropic efficiency (η_s).

Figure 17: Effect of w_P in the design of the parallel-type turbine-type device.

dency.

The convergence curves for the parallel-type turbine-type devices follow similar patterns as the convergence curve shown in Fig. 22 for the two-inlet turbine-type device.

The simulation of the optimized topology for the parallel-type turbine-type device for $w_P = 0.4$ (with power with the porosity term) is shown in Fig. 18.

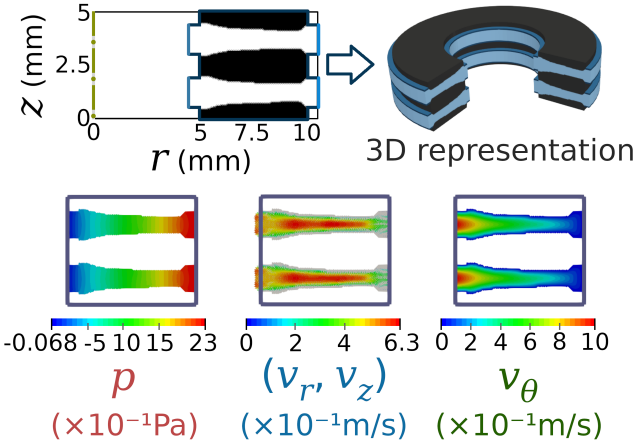

Figure 18: Optimized topology, 3D representation, pressure and velocity for the parallel-type turbine-type device ($w_P = 0.4$).

In Fig. 18, the fluid flow is shown to have some acceleration towards the outlet (at r_{ext}), which is consistent with the "Tesla principle" due to the wall rotation.

6.3. Effect of the rotation

The third example is the design of a two-inlet turbine-type device for different rotations (see Fig. 19): The computational domain is composed of two parabolic inlets located at the external radius r_{ext} (with imposed flow rates of $\frac{Q}{2}$, where Q is the "total" flow rate), and the outlet is axial. The specified volume fraction (f) is 70%.

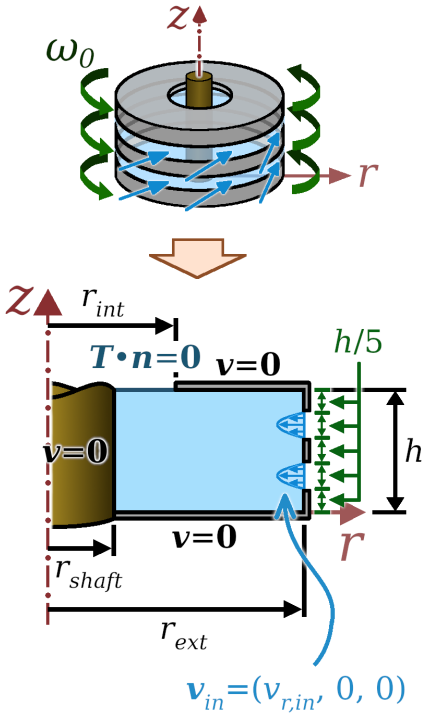

Figure 19: Design domain for the two-inlet turbine-type device.

The finite element mesh is chosen with 96 radial and 60 axial rectangular partitions of crossed triangular elements, totaling 11,677 nodes and 23,040 elements (see Fig. 20).

The input parameters and dimensions of the design domain that are used are shown in Table 3.

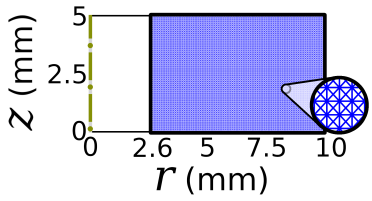

Figure 20: Mesh used for the two-inlet turbine-type device.

Table 3: Parameters used for the topology optimization of the two-inlet turbine-type device.

Input parameters	
Inlet flow rate (Q)	2.0 L/min
Rotation	$\omega_0 \neq 0$ rad/s
Inlet rotation	$\omega_{in} = \omega_0$
Radial-axial inlet velocity profile	Parabolic
Dimensions	
h	5 mm
r_{shaft}	2.6 mm
r_{int}	5 mm
r_{ext}	10 mm

A series of optimizations is performed for a sequence of rotations in order to evaluate the effect of the rotation in the design of the two-inlet turbine-type device. In this example, the objective function is the relative energy dissipation, and Fig. 21 shows the objective function (relative energy dissipation) values with respect to the rotation for each optimized topology. The objective function values that are shown correspond to the post-processed mesh. The maximum value for the maximum local Reynolds number ($\max(\mathrm{Re}_{\mathrm{ext},\,\ell})$) is given at 2000 rpm, as 3.07×10^3.

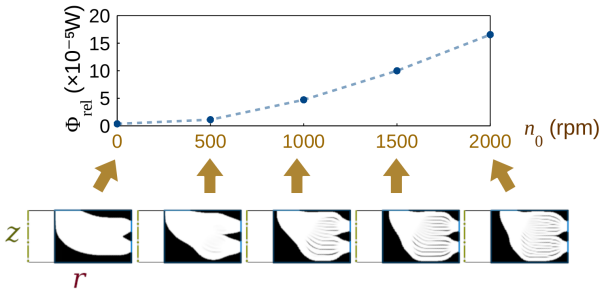

(a) Effect in the relative energy dissipation (Φ_{rel}).

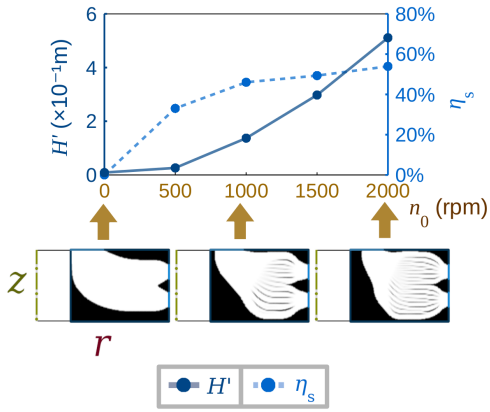

(b) Effect in the "turbine pressure head" ($H' = -H$) and isentropic efficiency (η_s).

Figure 21: Effect of the rotation in the design of the two-inlet turbine-type device.

As can be noticed in Fig. 21a, the number of intermediary "disk-like" structures seems to increase as the rotation increases. This can be explained by the fact that, when under rotation, the fluid flow concentrates itself near the solid surfaces due to the "Tesla principle". This means that having smaller fluid channels, such as in a size that is similar to the boundary layer, may possibly lead to less energy dissipation inside the fluid flow. Fig. 21 shows that the "turbine pressure head" (H') is higher under higher rotations, which means that the fluid exits the computational domain with even less energy than when it entered when under higher rotations. The rise in the isentropic efficiency (η_s) under higher rotations shows that the change in the "turbine pressure head" (H') value is accompanied by the fluid transfering more energy to the disks.

The optimization schemes for this example are shown in Table 4. The choice of the optimization parameters is performed for allowing the optimized topologies to be sufficiently discrete and also to block fluid flow (or at least significantly reduce it) inside the solid material (as in Alonso et al. [62]).

Table 4: Reference parameters for the optimization schemes (steps) for the two-inlet turbine-type device.

Rotation (n_0) (rpm)	$\kappa_{\max}$ ($\times 10^8 \mu$) (kg/(m^{3}s))	q
$0 \sim 1500$	1.0	10^3
2000	1.8	10^3

The convergence curve for the two-inlet turbine-type device for 1000 rpm is shown in Fig. 22.

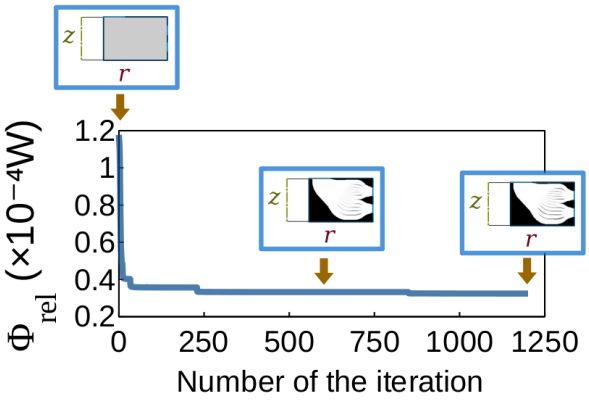

Figure 22: Convergence curve for the two-inlet turbine-type device (1000 rpm).

The simulation of the optimized topology for the two-inlet turbine-type device for 1000 rpm is shown in Fig. 23.

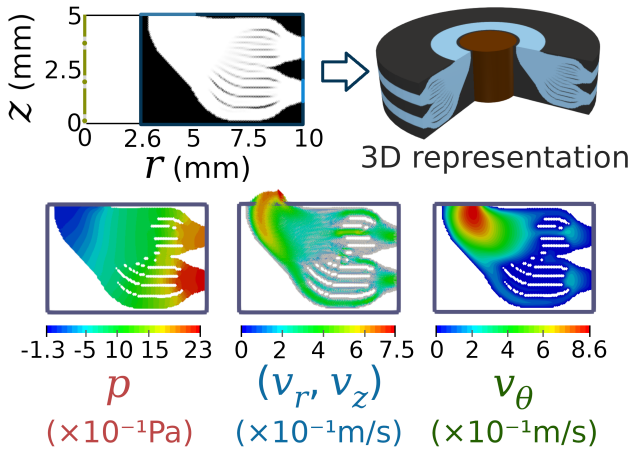

Figure 23: Optimized topology, 3D representation, pressure and velocity for the two-inlet turbine-type device (1000 rpm).

In the simulation shown in Fig. 23 for the two-inlet turbine-type device for 1000 rpm, the "Tesla principle" can be noticed from the "concentration" of radial-axial velocity vectors ((v_r, v_z)) between the "disk-like" structures. This can also be noticed for relative tangential velocity (v_θ), where v_θ is lower near the solid surfaces but higher farther from them. It can be noticed that, due to the higher radius of the rightmost part of the axial outlet, the absolute tangential velocity ($v_{\theta,\text{abs}} = v_\theta + \omega_0 r$) is higher, meaning that the outlet flow has a tendency to exit more intensely closer to this rightmost radius.

6.4. *Effect of the inlet rotation*

The fourth example is based on the tubular adhesion turbine concept [2], and is considered for different inlet rotations ($\omega_{in} \neq \omega_0$). The computational domain is composed of a parabolic inlet located at the external radius r_{ext}, and an outlet that is also located at the external radius r_{ext} (see Fig. 24). The specified volume fraction (f) is 70%.

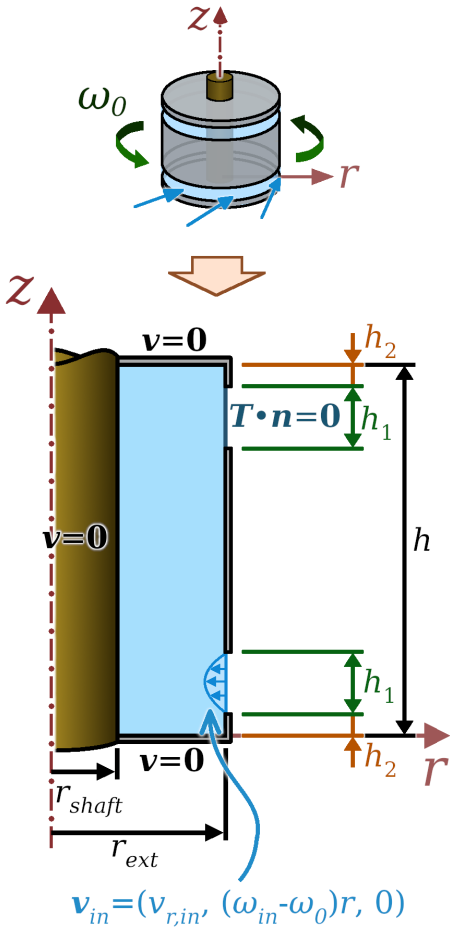

Figure 24: Design domain for the axial-type turbine-type device.

The finite element mesh is chosen with 30 radial and 100 axial rectangular partitions of crossed triangular elements, totaling 6,131 nodes and 12,000 elements (see Fig. 25). The input parameters and dimensions of the design domain that are used are shown in Table 5.

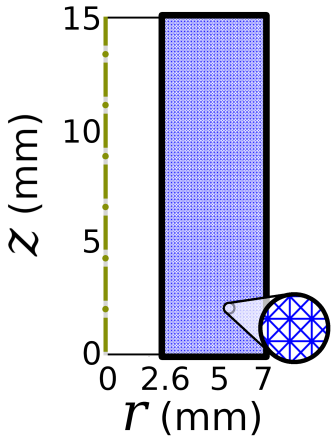

Figure 25: Mesh used for the axial-type turbine-type device.

Table 5: Parameters used for the topology optimization of the axial-type turbine-type device.

Input parameters	
Inlet flow rate (Q)	2.0 L/min
Rotation	$n_0 = 1000$ rpm
Inlet rotation	$\omega_{in} \neq \omega_0$
Radial-axial inlet velocity profile	Parabolic
Dimensions	
h	15 mm
h_1	2 mm
h_2	1 mm
r_{shaft}	2.6 mm
r_{ext}	7 mm

A series of optimizations is performed for a sequence of inlet rotations (ω_{in}) in order to evaluate its effect in the design of the axial-type turbine-type device. In this example, the objective function is the relative energy dissipation, and Fig. 26 shows the objective function (relative energy dissipation) values with respect to the inlet rotation for each optimized topology. The objective function values that are shown correspond to the post-processed mesh. The maximum value for the maximum local Reynolds number ($\max(\mathrm{Re}_{\mathrm{ext},\,\ell})$) is given at $n_{in} = 2000$ rpm, as 1.71×10^3.

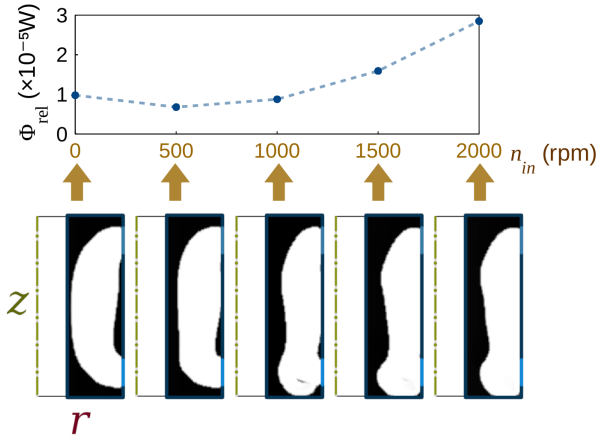

(a) Effect in the relative energy dissipation (Φ_{rel}).

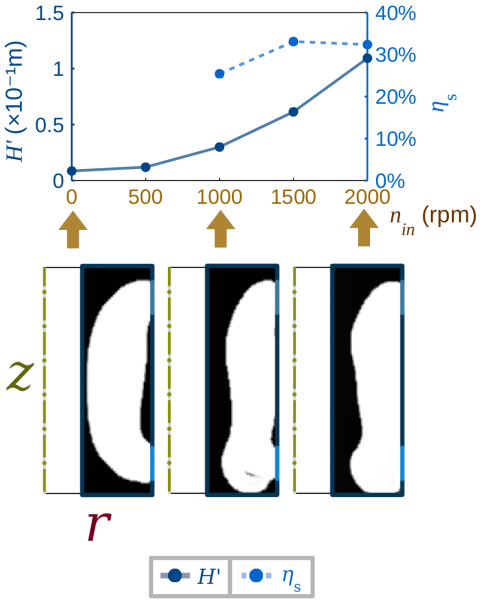

(b) Effect in the "turbine pressure head" ($H' = -H$) and isentropic efficiency (η_s).

Figure 26: Effect of the inlet rotation in the design of the axial-type turbine-type device.

In Fig. 26a, as the rotation increases, the fluid flow path distances itself from inner radii and attains an "inlet zone". This is probably because, respectively, (1) A fluid flow path at higher radii leads to more fluid flowing ((v_r, v_z)) under higher "swirl" velocities ($v_{\theta,\mathrm{abs}}$), and (2) Having an "inlet zone" seems to contribute to the change of the fluid flow direction and to lead the "swirl" component of the velocity ($v_{\theta,\mathrm{abs}}$) through the vertical fluid flow path. It can be highlighted that, for inlet rotations that are smaller than the wall rotation (i.e., for $\omega_{in} < \omega_0$), the fluid flow device does not act as a turbine and neither as a pump. This may be understood by the reasoning that the inlet fluid should enter a turbine-type device with at least the same rotation of the turbine-type device, otherwise it would be unable to transfer energy to the device, resulting in a "brake"-like behavior, only dissipating energy. This

can be noticed in Fig. 26b, where the efficiency values for 0 rpm and 500 rpm inlet rotations are not shown, because these inlet rotations are unable to transfer power to the solid structure (i.e., the values of "turbine power" (P'_f) are negative), meaning that the fluid device does not act as a turbine. Also, since the "turbine pressure head" (H') is positive, it also does not act as a pump.

The optimization schemes for this example are shown in Table 6.

Table 6: Reference parameters for the optimization schemes (steps) for the axial-type turbine-type device.

Inlet rotation (n_{in}) (rpm)	$\kappa_{\max}$ ($\times 10^8 \mu$) (kg/(m^{3}s))	q
$0 \sim 500$	80	10^3
$1000 \sim 1500$	2.5	10^3
2000	5.0	10^3

The convergence curves for the axial-type turbine-type devices follow similar patterns as the convergence curve shown in Fig. 22 for the two-inlet turbine-type device.

The simulation of the optimized topology for the axial-type turbine-type device for 2000 rpm is shown in Fig. 27.

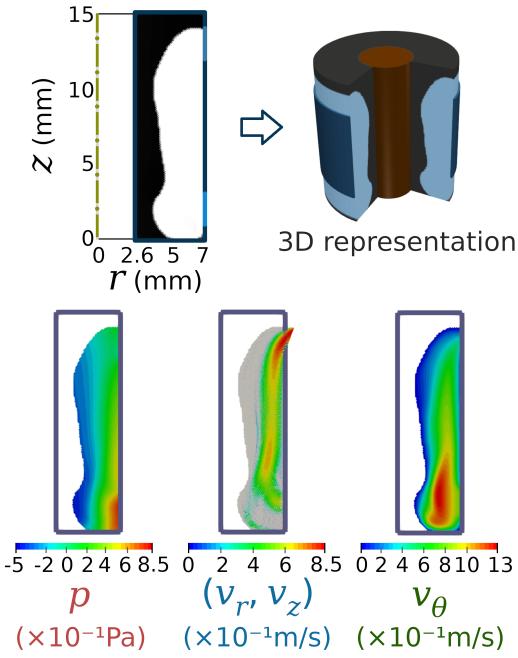

Figure 27: Optimized topology, 3D representation, pressure and velocity for the axial-type turbine-type device (2000 rpm inlet rotation).

Fig. 27 shows that the radial-axial ((v_r, v_z)) velocity mainly follows a single fluid flow path inside the channel, while the relative tangential velocity (v_θ) shows some acceleration when the fluid enters the channel. This accelerated fluid is then decelerated through the vertical fluid path, while transfering energy to the solid walls.

6.5. Effect of the specified fluid volume fraction

The last example is the design of a one-inlet turbine-type device by considering different specified fluid volume fractions in the fluid volume constraint (see Fig. 28): The computational domain is composed of one parabolic inlet located at the external radius r_{ext}, and the outlet is axial.

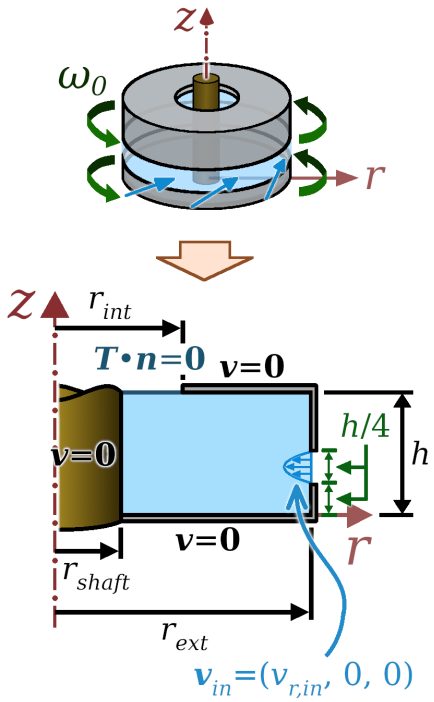

Figure 28: Design domain for the one-inlet turbine-type device.

The finite element mesh is the same shown in Fig. (20). The input parameters and dimensions of the design domain that are used are shown in Table 7. The optimization scheme for this example is given by $\kappa_{\max} = 5.0 \times 10^8 \mu$ (kg/(m^{3}s)) and $q = 10^3$.

Table 7: Parameters used for the topology optimization of the one-inlet turbine-type device.

Input parameters	
Inlet flow rate (Q)	2.0 L/min
Rotation	$n_0 = 1000$ rpm
Inlet rotation	$\omega_{in} = \omega_0$
Radial-axial inlet velocity profile	Parabolic
Dimensions	
h	5 mm
r_{shaft}	2.6 mm
r_{int}	5 mm
r_{ext}	10 mm

A series of optimizations is performed for a sequence of specified volume fractions in order to evaluate its effect in the design of the one-inlet turbine-type device. In this example, the objective function is the relative energy dissipation, and Fig. 29 shows the objective function (relative energy dissipation) values with respect to the specified volume fraction for each optimized topology. The objective function values that are shown correspond to the post-processed mesh. The maximum value for the maximum local Reynolds number ($\max(\mathrm{Re}_{\mathrm{ext},\,\ell})$) is given as 3.1×10^3.

In Fig. 29a, it can be noticed that, as the specified volume fraction is increased, the number of "disk-like" structures also increases until $f = 70\%$, from when the "outer shape" starts to significantly change. The formation of these "disk-like" structures is seemingly to reduce the size of the flow paths to an adequate size according to the "Tesla principle", as in the case mentioned in Section 6.3. The "outer shape" starts changing due to the specified volume fraction allowing more fluid in the design domain, which leads the topology optimization to achieve these different formats.

Fig. 29a shows that, for $f \geqslant 50\%$, the energy dissipation shows small difference between the different optimized topologies. The results for $f = 10\%$ are not evaluated because the amount of fluid allowed is too small for the given design, and the fluid flow path is completely blocked. The result for $f = 100\%$ corresponds to not using the volume constraint. It can also be highlighted that the optimized topologies for $f = 90\%$ and $f = 100\%$ still feature "gray regions" which could not be removed by changing the material model parameters and neither by including a filter or projection (such as a Helmholtz filter [105]). The effect when including a Helmholtz filter (PDE-based filter) or even an algebraic-based filter [106] is that the intermediary structures stay as "gray material", but have their leftmost ends joined by a "thin gray material".

By checking the isentropic efficiency (η_s) in Fig. 29b, it can be noticed that the optimized topologies for $f = 60\%$ and $f = 70\%$ feature the highest values. By comparing the "turbine pressure head" (H'), it can be noticed that it is slightly higher for $f = 60\%$, which may possibly mean that this optimized topology is seemingly better than the $f = 70\%$ topology.

The convergence curves for the one-inlet turbine-type devices follow similar patterns as the convergence curve shown in Fig. 22 for the two-inlet turbine-type device.

The simulation of the optimized topology for the one-inlet turbine-type device for $f = 60\%$ is shown in Fig. 30.

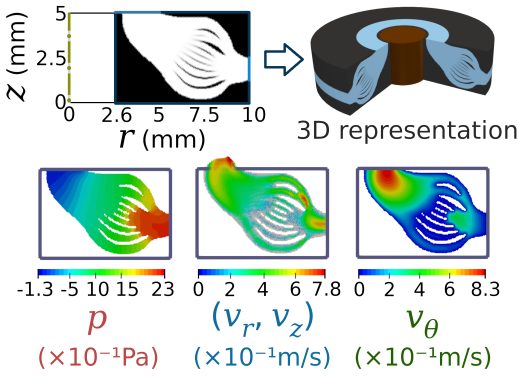

Figure 30: Optimized topology, 3D representation, pressure and velocity for the one-inlet turbine-type device ($f = 60\%$).

In Fig. 30, it can be noticed that the radial-axial inlet flow ((v_r, v_z)) is divided between the various "disk-like" structures, and concentrates itself closer to the upper and lower borders of the "outer shape" of the topology. Also, the relative tangential velocity (v_θ) includes some acceleration in the middle of the fluid paths, which is due to the "Tesla principle".

6.6. Post-processing of the numerical results for fabrication

When considering the fabrication of Tesla turbine devices, it is necessary to consider spacers/arms (Fig. 3). In the case of the optimized topologies for the Tesla turbine, this same concept can be applied, but with the pins/spacers serving as connectors between disks, rather than relying on single straight bolts that traverse all disks (Fig. 3). This is shown in Fig. 31, for an example optimized topology, in order to facilitate visualization. First, there is an example optimized topology obtained from the 2D swirl flow model, which can be represented in 3D as shown next. Following, there is an additional design step, which consists of including the spacers/arms, requiring the design choice/analysis of their disposition, size and shape/geometry so as to minimize their influence in the fluid flow, while also taking material constraints (such as resistance) into account. This additional step is out of the scope of this work, but some possibilities are shown in Fig. 31: circular pins may be chosen as the spacers, while spaced by 120° angles (Fig. 31a); outlet arms may also be

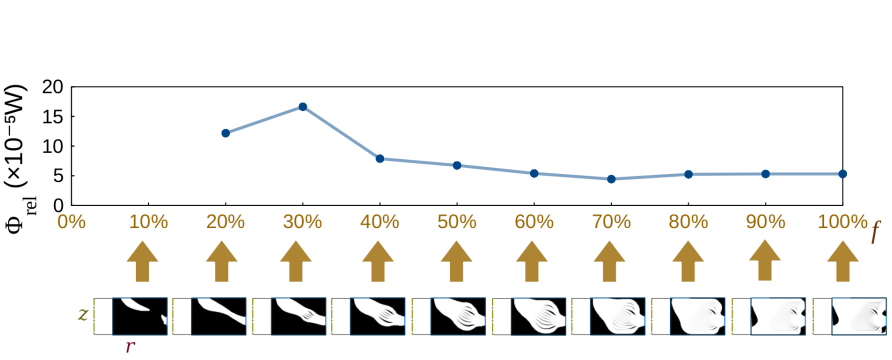

(a) Effect in the relative energy dissipation (Φ_{rel}).

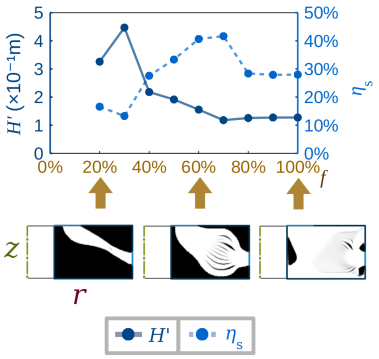

(b) Effect in the "turbine pressure head" ($H' = -H$) and isentropic efficiency (η_s).

Figure 29: Effect of the specified volume fraction in the design of the one-inlet turbine-type device.

included (Fig. 31b); the 120° spaced circular pins may be "intercalated" between each pair of disks, featuring, for example, some intermediary pins at 0°-120°-240° and others at 60°-180°-300° (Fig. 31c); the 120° spaced circular pins may be reinforced by adding some more pins (Fig. 31d); other spacings between pins, such as 90°, may be considered (Fig. 31e); and other spacer shapes/geometries may be considered, such as airfoil-shaped spacers (Fig. 31f). In terms of fabrication, depending on the scale of the optimized topology, the corresponding prototype may be fabricated as a single part through additive manufacturing. In larger dimensions, the spacers and disks may be even fabricated through conventional means (such as through stamping and machining), with bolts between each pair of disks in order to fixate the spacers and disks.

7. Conclusions

This work presents a topology optimization approach for the design of Tesla-type turbine devices, by considering various aspects: the 2D swirl flow model, due to its smaller computational cost in relation to a complete 3D model; MINI elements, in order to reduce the computational cost from using Taylor-Hood elements (due to the possible need of higher resolution meshes to attain the disk-like structures in the optimized topologies); the Brinkman-Forchheimer model, which includes an additional inertial effect in the material model that may lead to better optimized 2D swirl flow turbine designs; and a power objective function with an additional porosity effect term. All these aspects are necessary to achieve a successful topology optimization for simulation for designing 2D swirl flow turbine-type devices (i.e., Tesla turbines).

The numerical examples show the different aspects considered in the design separately: the Brinkman-Forchheimer model, the power objective function, the rotation, the inlet rotation, and the specified fluid volume fraction. By applying the topology optimization method, "disk-like" structures appear in order to improve the performance of the fluid flow device, which depend on rotation / inlet rotation, the definition of the material model, and the design domain. The power objective function formulation including the additional porosity effect term is more consistent with respect to the relative energy dissipation definition, although, when combined with energy dissipation in an objective function, its effect may lead to worse local minima.

In terms of the intermediary disk-like structures of the optimized topologies, the same approach described above should be followed, with circumferentially-spaced spacers or arms. In terms of manufacturing, the device may be manufactured through additive manufacturing, or even conventional means, as mentioned in Section 6.6. It can be highlighted that additive manufacturing is able to fabricate highly detailed and complex structures, such as the complex "super-truss"-structures from Liu et al. [107].

As future work, it is suggested to optimize for thermal flows, non-Newtonian fluid flows and turbulence models.

Acknowledgements

This research was partly supported by CNPq (Brazilian Research Council) and FAPESP (São Paulo Research Foundation). The authors thank the supporting institutions. The first author thanks the financial support of FAPESP under grant 2017/27049-0. The second author thanks the financial support of CNPq (National Council for Research and Development) under grant 302658/2018-1 and of FAPESP under grant 2013/24434-0. The authors also acknowledge the support of the RCGI (Research Centre for Greenhouse Gas Innovation), hosted by the University of São Paulo (USP) and sponsored by FAPESP (2014/50279-4) and Shell Brazil.

Declarations of interest

None.

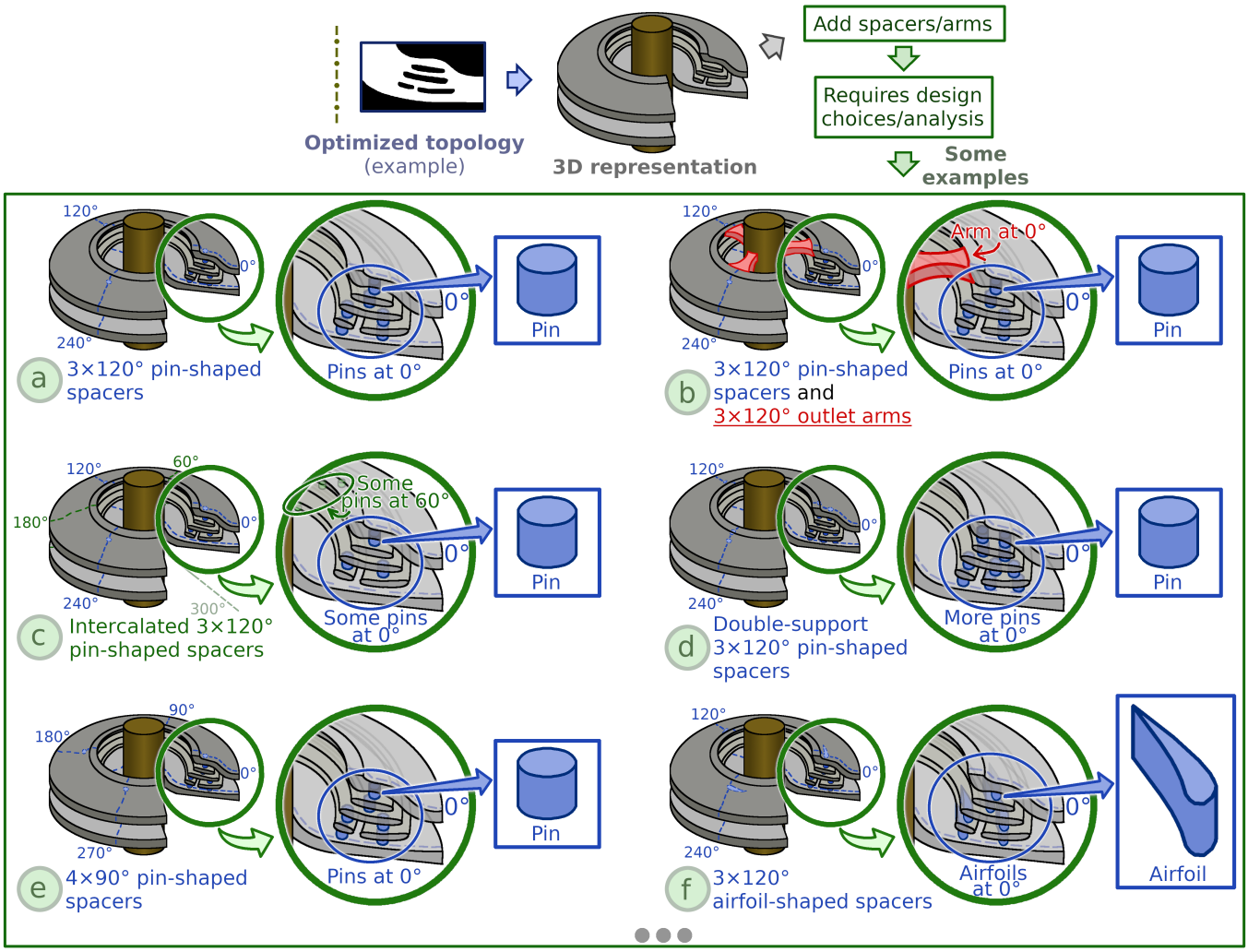

Figure 31: Some spacer/arm configurations illustrated for an example optimized topology. The Tesla turbine rotor is shown in a 320° section, for illustrative purposes

References

1. Tesla N. Turbine. 1913. US 1,061,206.
2. Ford D. Tubular adhesion turbine or pump. 2018. US 15/742,444.
3. Shi J. Filamentous turbine. 2016. US 9.260,967 B2.
4. Hui JY. Combined electricity, heat, and chill generation for a rankine engine. 2018. US 10/001,025.
5. Hoya GP, Guha A. The design of a test rig and study of the performance and efficiency of a tesla disc turbine. *Proceedings of the Institution of Mechanical Engineers, Part A: Journal of Power and Energy* 2009;223(4):451–65. URL: https://doi.org/10.1243/09576509JPE664. doi:10.1243/09576509JPE664. arXiv:https://doi.org/10.1243/09576509JPE664.
6. Sengupta S, Guha A. A theory of tesla disc turbines. *Proceedings of the Institution of Mechanical Engineers, Part A: Journal of Power and Energy* 2012;226(5):650–63. URL: https://doi.org/10.1177/0957650912446402. doi:10.1177/0957650912446402. arXiv:https://doi.org/10.1177/0957650912446402.
7. Rey Ladino AF. Numerical simulation of the flow field in a friction-type turbine (tesla turbine). Diploma thesis; Institute of Thermal Powerplants, Vienna University of Technology; 2004.
8. Jose R, Jose A, Benny A, Salus A, Benny B. An experimental study on the various parameters of tesla turbine using cfd. *International Advanced Research Journal in Science, Engineering and Technology* 2016;3(3):2394–1588.
9. Bloudíček P, Paloušek D. Design of tesla turbine. In: *Konference diplomových prací 2007*. 2007:.
10. Choon TW, Rahman. AA, Jer FS, Aik LE. Optimization of tesla turbine using computational fluid dynamics approach. In: *2011 IEEE Symposium on Industrial Electronics and Applications*. 2011:477–80. doi:10.1109/ISIEA.2011.6108756.
11. Ho-Yan BP. Tesla turbine for pico hydro applications. *Guelph Engineering Journal* 2011;4:1–8.
12. Ritzi EW. Multi-stage, wet steam turbine. 1981. US 4,258,551.
13. Baik S, Heo JY, Kwon J, Lee JI. Preliminary study of friction disk type turbine for s-co2 cycle application. In: *The Korean Nuclear Society Autumn Meeting*. The Korean Nuclear Society; 2016:.
14. Borrvall T, Petersson J. Topology optimization of fluids in stokes flow. *International Journal for Numerical Methods in Fluids* 2003;41(1):77–107. URL: http://dx.doi.org/10.1002/fld.426. doi:10.1002/fld.426.
15. Duan X, Li F, Qin X. Topology optimization of incompressible navier–stokes problem by level set based adaptive mesh method. *Computers & Mathematics with Applications* 2016;72(4):1131 –41. URL: http://www.sciencedirect.com/science/article/pii/S0898122116303662. doi:https://doi.org/10.1016/j.camwa.2016.06.034.
16. Duan X, Qin X, Li F. Topology optimization of stokes flow using an implicit coupled level set method. *Applied Mathematical Modelling* 2016;40(9):5431–41. URL: https://www.sciencedirect.com/science/article/pii/S0307904X16000044. doi:https://doi.org/10.1016/j.apm.2015.12.040.
17. Zhou S, Li Q. A variationals level set method for the topology optimization of steady-state navier–stokes flow. *Journal of Computational Physics* 2008;227(24):10178–95.
18. Sokolowski J, Zochowski A. On the topological derivative in shape optimization. *SIAM journal on control and optimization* 1999;37(4):1251–72.
19. Sá LFN, Amigo RCR, Novotny AA, Silva ECN. Topological derivatives applied to fluid flow channel design optimization problems. *Structural and Multidisciplinary Optimization* 2016;54(2):249–64. URL: https://doi.org/10.1007/s00158-016-1399-0. doi:10.1007/s00158-016-1399-0.
20. Evgrafov A. Topology optimization of navier-stokes equations. In: *Nordic MPS 2004. The Ninth Meeting of the Nordic Section of the Mathematical Programming Society*. 014; Linköping University Electronic Press; 2004:37–55.
21. Olesen LH, Okkels F, Bruus H. A high-level programming-language implementation of topology optimization applied to steady-state navier–stokes flow. *International Journal for Numerical Methods in Engineering* 2006;65(7):975–1001.
22. Evgrafov A. Topology optimization of slightly compressible fluids. *ZAMM-Journal of Applied Mathematics and Mechanics/Zeitschrift für Angewandte Mathematik und Mechanik* 2006;86(1):46–62.
23. Sá LFN, Okubo Jr CM, Silva ECN. Topology optimization of subsonic compressible flows. *Structural and Multidisciplinary Optimization* 2021;Accepted for publication.
24. Guest JK, Prévost JH. Topology optimization of creeping fluid flows using a darcy–stokes finite element. *International Journal for Numerical Methods in Engineering* 2006;66(3):461–84. URL: http://dx.doi.org/10.1002/nme.1560. doi:10.1002/nme.1560.
25. Wiker N, Klarbring A, Borrvall T. Topology optimization of regions of darcy and stokes flow. *International journal for numerical methods in engineering* 2007;69(7):1374–404.
26. Pingen G, Maute K. Optimal design for non-newtonian flows using a topology optimization approach. *Computers & Mathematics with Applications* 2010;59(7):2340–50.
27. Hyun J, Wang S, Yang S. Topology optimization of the shear thinning non-newtonian fluidic systems for minimizing wall shear stress. *Computers & Mathematics with Applications* 2014;67(5):1154 –70. URL: http://www.sciencedirect.com/science/article/pii/S0898122113007074. doi:https://doi.org/10.1016/j.camwa.2013.12.013.
28. Sato Y, Yaji K, Izui K, Yamada T, Nishiwaki S. An optimum design method for a thermal-fluid device incorporating multiobjective topology optimization with an adaptive weighting scheme. *Journal of Mechanical Design* 2018;140(3):031402.
29. Ramalingom D, Cocquet PH, Bastide A. A new interpolation technique to deal with fluid-porous media interfaces for topology optimization of heat transfer. *Computers & Fluids* 2018;168:144 –58. URL: http://www.sciencedirect.com/science/article/pii/S0045793018301932. doi:https://doi.org/10.1016/j.compfluid.2018.04.005.
30. Lv Y, Liu S. Topology optimization and heat dissipation performance analysis of a micro-channel heat sink. *Meccanica* 2018;53(15):3693–708.
31. Yoon GH. Topology optimization for turbulent flow with spalart–allmaras model. *Computer Methods in Applied Mechanics and Engineering* 2016;303:288 – 311. URL: http://www.sciencedirect.com/science/article/pii/S004578251630007X. doi:https://doi.org/10.1016/j.cma.2016.01.014.
32. Dilgen CB, Dilgen SB, Fuhrman DR, Sigmund O, Lazarov BS. Topology optimization of turbulent flows. *Computer Methods in Applied Mechanics and Engineering* 2018;331:363–393. doi:10.1016/j.cma.2017.11.029.
33. Sá LF, Yamabe PV, Souza BC, Silva EC. Topology optimization of turbulent rotating flows using spalart–allmaras model. *Computer Methods in Applied Mechanics and Engineering* 2021;373:113551. URL: http://www.sciencedirect.com/science/article/pii/S0045782520307362. doi:https://doi.org/10.1016/j.cma.2020.113551.
34. Nørgaard S, Sigmund O, Lazarov B. Topology optimization of unsteady flow problems using the lattice boltzmann method. *J Comput Phys* 2016;307(C):291–307. URL: https://doi.org/10.1016/j.jcp.2015.12.023. doi:10.1016/j.jcp.2015.12.023.
35. Hasund KES. Topology optimization for unsteady flow with applications in biomedical flows. Master's thesis; NTNU; 2017.
36. Song XG, Wang L, Baek SH, Park YC. Multidisciplinary optimization of a butterfly valve. *ISA transactions* 2009;48(3):370–7.
37. Sato Y, Yaji K, Izui K, Yamada T, Nishiwaki S. Topology optimization of a no-moving-part valve incorporating pareto frontier exploration. *Struct Multidiscip Optim* 2017;56(4):839–51. URL: https://doi.org/10.1007/s00158-017-1690-8. doi:10.

1007/s00158-017-1690-8.
38. Jensen KE, Szabo P, Okkels F. Topology optimizatin of viscoelastic rectifiers. *Applied Physics Letters* 2012;100(23):234102.
39. Andreasen CS, Gersborg AR, Sigmund O. Topology optimization of microfluidic mixers. *International Journal for Numerical Methods in Fluids* 2009;61:498–513. URL: http://dx.doi.org/10.1002/fld.1964.
40. Deng Y, Zhou T, Liu Z, Wu Y, Qian S, Korvink JG. Topology optimization of electrode patterns for electroosmotic micromixer. *International Journal of Heat and Mass Transfer* 2018;126:1299–315.
41. Romero J, Silva E. A topology optimization approach applied to laminar flow machine rotor design. *Computer Methods in Applied Mechanics and Engineering* 2014;279(Supplement C):268 – 300. URL: http://www.sciencedirect.com/science/article/pii/S0045782514002151. doi:https://doi.org/10.1016/j.cma.2014.06.029.
42. Romero JS, Silva ECN. Non-newtonian laminar flow machine rotor design by using topology optimization. *Structural and Multidisciplinary Optimization* 2017;55(5):1711–32.
43. Zhang B, Liu X, Sun J. Topology optimization design of non-newtonian roller-type viscous micropumps. *Structural and Multidisciplinary Optimization* 2016;53(3):409–24.
44. Ko J. Numerical modelling of highly swirling flows in a cylindrical through-flow hydrocyclone. Ph.D. thesis; KTH; 2005.
45. Susan-Resiga RF, Muntean S, Tănasă C, Bosioc A. Three-dimensional versus two-dimensional axisymmetric analysis for decelerated swirling flows. In: *Conference on Modelling Fluid Flow (CMFF'06)*. Department of Fluid Mechanics, Faculty of Mechanical Engineering, Budapest University of Technology and Economics; 2006:.
46. Holland K. Design, construction and testing of a tesla turbine. Master's thesis; The Faculty of Graduate Studies, Laurentian University; 2015.
47. Polisetti S, Venkatraman S, Miryala M. Fabrication and study of the parameters affecting the efficiency of a bladeless turbine. 2017:78–82.
48. Krishnan V. Design and fabrication of cm-scale tesla turbines. Master's thesis; Electrical Engineering and Computer Sciences, University of California at Berkeley; 2015.
49. Li R, Wang H, Yao E, Li M, Nan W. Experimental study on bladeless turbine using incompressible working medium. *Advances in Mechanical Engineering* 2017;9(1):1687814016686935.
50. Dodsworth L. Operational parametric study of a prototype tesla pump. Master's thesis; Dalhousie University; 2016.
51. Beans EW. Investigation into the performance characteristics of a friction turbine. *Journal of Spacecraft and Rockets* 1966;3(1):131–4.
52. Leaman AB. The design, construction and investigation of a tesla turbine. Ph.D. thesis; University of Maryland; 1950.
53. Motin A. Theoretical and numerical study of swirling flow separation devices for oil-water mixtures. Ph.D. thesis; Michigan State University; 2015.
54. Paladino E, Aguirre Ja, Quintella E. Developing multiphase models for liquid-liquid hydrocyclone flow. In: *6th International Conference on Multiphase Flow, S6 Wed C*; vol. 37. 2007:.
55. Osei H, Al-Kayiem H, Ahmed O. Flow dynamics behaviour of a novel liquid-liquid hydrocyclone with varying upper cylindrical lengths and number of inlets. *ARPN J Eng Appl Sci* 2016;11:12159–64.
56. Amini G. Liquid flow in a simplex swirl nozzle. *International Journal of Multiphase Flow* 2016;79:225–35.
57. Hallgren L, Takagi S, Tilliander A, Yokoya S, Jönsson P. Effect of nozzle type and swirl on flow pattern for initial filling conditions in the mould for up-hill teeming. *steel research international* 2007;78(3):254–9.
58. Eslamian E, Shirvani H, Shirvani A. Numerical investigation of swirl flow inside a supersonic nozzle. *Adv Fluid Mech IX* 2012;74:131–40.
59. Zhang H, Jia X, Pan X, Jiang B, Zheng Q. Interaction between rotor and annular seals: interlaced and straight-through labyrinth seals. *Journal of Propulsion and Power* 2016;32(6):1483–93.
60. Bellaouar A, Kopey B, Abdelbaki N. Methods of the rational choice of a labyrinth seal design for gas pumping unit. *Mechanics* 2013;19(1):81–6.
61. Tesla N. Fluid propulsion. 1913. US Patent 1,061,142.
62. Alonso DH, de Sá LFN, Saenz JSR, Silva ECN. Topology optimization applied to the design of 2d swirl flow devices. *Structural and Multidisciplinary Optimization* 2018;58(6):2341–64. URL: https://doi.org/10.1007/s00158-018-2078-0. doi:10.1007/s00158-018-2078-0.
63. Alonso DH, de Sá LFN, Saenz JSR, Silva ECN. Topology optimization based on a two-dimensional swirl flow model of tesla-type pump devices. *Computers & Mathematics with Applications* 2019;77(9):2499 –533. URL: http://www.sciencedirect.com/science/article/pii/S0898122118307338. doi:https://doi.org/10.1016/j.camwa.2018.12.035.
64. Darcy HPG. Les Fontaines publiques de la ville de Dijon. Exposition et application des principes à suivre et des formules à employer dans les questions de distribution d'eau, etc. V. Dalamont; 1856.
65. Forchheimer P. Wasserbewegung durch boden. *Z Ver Deutsch, Ing* 1901;45:1782–8.
66. Philippi B, Jin Y. Topology optimization of turbulent fluid flow with a sensitive porosity adjoint method (spam). *arXiv:151208445* 2015;.
67. Arnold D, Brezzi F, Fortin M. A stable finite element method for the stokes equations. *Calcolo* 1984;21:337–44.
68. Munson BR, Young DF, Okiishi TH. Fundamentals of fluid mechanics. 6 ed.; John Wiley & Sons, Inc.; 2009.
69. White FM. Fluid Mechanics. 7 ed.; McGraw-Hill, 2011; 2009.
70. Reddy JN, Gartling DK. The finite element method in heat transfer and fluid dynamics. 3 ed.; CRC press; 2010.
71. Langtangen HP, Logg A. Solving PDEs in Minutes – The FEniCS Tutorial Volume I. 2016. URL: https://fenicsproject.org/book/.
72. Girault V, Raviart P. Finite Element Methods for Navier-Stokes Equations: Theory and Algorithms. Springer Series in Computational Mathematics; Springer Berlin Heidelberg; 2012. ISBN 9783642616235.
73. Guzmán J, Salgado AJ, Sayas FJ. A note on the ladyženskaja-babuška-brezzi condition. *J Sci Comput* 2013;56(2):219–29. URL: http://dx.doi.org/10.1007/s10915-012-9670-z. doi:10.1007/s10915-012-9670-z.
74. Brezzi F, Fortin M. Mixed and Hybrid Finite Element Methods. Berlin, Heidelberg: Springer-Verlag; 1991. ISBN 0-387-97582-9.
75. Logg A, Mardal KA, Wells G. Automated solution of differential equations by the finite element method: The FEniCS book; vol. 84. Springer Science & Business Media; 2012. URL: https://fenicsproject.org/book/.
76. Elhanafy A, Guaily A, Elsaid A. Pressure stabilized finite elements simulation for steady and unsteady newtonian fluids. *Journal of Applied Mathematics and Computational Mechanics* 2017;16(3):17–26.
77. Langtangen HP, Mardal KA, Winther R. Numerical methods for incompressible viscous flow. *Advances in water Resources* 2002;25(8-12):1125–46.
78. Franca LP. Stabilized finite element methods: Ii. the incompressible navier-stokes equations. *Computer Methods in Applied Mechanics and Engineering* 1992;99(258):209–33.
79. Brinkman HC. A calculation of the viscous force exerted by a flowing fluid on a dense swarm of particles. *Journal of applied sciences research* 1947;A1:27–34.
80. Huang H, Ayoub JA. Applicability of the forchheimer equation for non-darcy flow in porous media. In: *SPE Annual Technical Conference and Exhibition*. Society of Petroleum Engineers;

2006:.
81. Alimohamadi H, Imani M, Shojaeizadeh M. Numerical simulation of porosity effect on blood flow pattern and atherosclerotic plaques temperature. *International journal of technology enhancements and emerging engineering research* 2014;2(10).
82. Geertsma J. Estimating the coefficient of inertial resistance in fluid flow through porous media. *Society of Petroleum Engineers Journal* 1974;14(05):445–50.
83. Lasseux D, Valdés-Parada FJ. On the developments of darcy's law to include inertial and slip effects. *Comptes Rendus Mécanique* 2017;345(9):660 –9. URL: http://www.sciencedirect.com/science/article/pii/S1631072117300979. doi:https://doi.org/10.1016/j.crme.2017.06.005; a century of fluid mechanics: 1870–1970.
84. Kundu P, Kumar V, Mishra IM. Experimental and numerical investigation of fluid flow hydrodynamics in porous media: Characterization of pre-darcy, darcy and non-darcy flow regimes. *Powder Technology* 2016;303:278–91.
85. Wang L, Torres A, Xiang L, Fei X, Naido A, Wu W. A technical review on shale gas production and unconventional reservoirs modeling. *Natural Resources* 2015;6(03):141.
86. Bear J. Modeling Phenomena of Flow and Transport in Porous Media; vol. 31. Springer; 2018.
87. Joseph DD, Nield DA, Papanicolaou G. Nonlinear equation governing flow in a saturated porous medium. *Water Resources Research* 1982;18(4):1049–52. URL: https://agupubs.onlinelibrary.wiley.com/doi/abs/10.1029/WR018i004p01049. doi:10.1029/WR018i004p01049. arXiv:https://agupubs.onlinelibrary.wiley.com/doi/pdf/10.1029/WR018i004p01049.
88. Vafai K. Handbook of porous media. 2 ed.; Crc Press; 2005.
89. Cimolin F, Discacciati M. Navier–stokes/forchheimer models for filtration through porous media. *Applied Numerical Mathematics* 2013;72:205–24.
90. Beavers GS, Sparrow EM. Non-darcy flow through fibrous porous media. *Journal of Applied Mechanics* 1969;36:711–4. doi:10.1115/1.3564760.
91. Shwartz J, Probstein RF. Experimental study of slurry separators for use in desalination. *Desalination* 1969;6(2):239 –66. URL: http://www.sciencedirect.com/science/article/pii/001191646980007X. doi:https://doi.org/10.1016/0011-9164(69)80007-X.
92. Ward JC. Turbulent flow in porous media. *Journal of the Hydraulics Division* 1964;90(5):1–12.
93. Varsakelis C, Papalexandris MV. On the well-posedness of the darcy–brinkman–forchheimer equations for coupled porous media-clear fluid flow. *Nonlinearity* 2017;30(4):1449–64. URL: https://doi.org/10.1088%2F1361-6544%2Faa5ecf. doi:10.1088/1361-6544/aa5ecf.
94. Tosco T, Marchisio DL, Lince F, Sethi R. Extension of the darcy–forchheimer law for shear-thinning fluids and validation via pore-scale flow simulations. *Transport in Porous Media* 2013;96(1):1–20. URL: https://doi.org/10.1007/s11242-012-0070-5. doi:10.1007/s11242-012-0070-5.
95. Amigo RCR, Prado DS, Paiva JL, Hewson RW, Silva ECN. Topology optimisation of biphasic adsorbent beds for gas storage. *Structural and Multidisciplinary Optimization* 2018;58(6):2431–54. URL: https://doi.org/10.1007/s00158-018-2117-x. doi:10.1007/s00158-018-2117-x.
96. Whitaker S. The forchheimer equation: A theoretical development. *Transport in Porous Media* 1996;25(1):27–61. URL: https://doi.org/10.1007/BF00141261. doi:10.1007/BF00141261.
97. Farrell PE, Ham DA, Funke SW, Rognes ME. Automated derivation of the adjoint of high-level transient finite element programs. *SIAM Journal on Scientific Computing* 2013;35(4):C369–93.
98. Mitusch S, Funke S, Dokken J. dolfin-adjoint 2018.1: automated adjoints for fenics and firedrake. *Journal of Open Source Software* 2019;4(38):1292. URL: https://doi.org/10.21105/joss.01292.
99. Wächter A, Biegler LT. On the implementation of an interior-point filter line-search algorithm for large-scale nonlinear programming. *Mathematical programming* 2006;106(1):25–57.
100. Amestoy PR, Duff IS, Koster J, L'Excellent JY. A fully asynchronous multifrontal solver using distributed dynamic scheduling. *SIAM Journal on Matrix Analysis and Applications* 2001;23(1):15–41.
101. The Engineering Toolbox . Air - dynamic and kinematic viscosity. 2019. URL: https://www.engineeringtoolbox.com/air-absolute-kinematic-viscosity-d_601.html.
102. Sonntag RE, Borgnakke C. Fundamentals of Thermodynamics. 8 ed.; Wiley; 2013.
103. Sabersky RH, Acosta AJ, Hauptmann EG, Gates EM. Fluid flow: a first course in fluid mechanics; vol. 299. Macmillan; 1971.
104. Wu J. Letter to the editor: A possible major mistake in the paper entitled "collected nondimensional performance of rotary dynamic blood pump": Smith wa, allaire p, antaki j, butler kc, kerkhoffs w, kink t, loree h, reul h. asaio journal 50: 25–32, 2004. *Asaio Journal* 2007;53(2):255–6.
105. Lazarov BS, Sigmund O. Filters in topology optimization based on helmholtz-type differential equations. *International Journal for Numerical Methods in Engineering* 2010;86(6):765–81.
106. Almeida SRM, Paulino GH, Silva ECN. Layout and material gradation in topology optimization of functionally graded structures: a global–local approach. *Structural and Multidisciplinary Optimization* 2010;42(6):855–68. URL: https://doi.org/10.1007/s00158-010-0514-x. doi:10.1007/s00158-010-0514-x.
107. Liu J, Yu H, To A. Porous structure design through blinn transformation-based level set method. *Structural and Multidisciplinary Optimization* 2018;57:1–16. doi:10.1007/s00158-017-1786-1.

Appendix A. Relationship between energy dissipation and pressure head

In order to derive the relationship between energy dissipation and pressure head, the differential equation that corresponds the Navier-Stokes equations (eq. (2)) is multiplied by $\boldsymbol{v}$ and integrated over the computational domain ($2\pi rd\Omega$). The resulting equation after considering zero external body forces and applying Gauss's divergence theorem in the divergent of the stress tensor becomes

$$\begin{aligned}\mathbf{0} = &\int_\Omega [\rho\nabla\boldsymbol{v}\bullet\boldsymbol{v} + 2\rho(\boldsymbol{\omega}\wedge\boldsymbol{v}) \\ &+ \rho\boldsymbol{\omega}\wedge(\boldsymbol{\omega}\wedge\boldsymbol{r})]\bullet\boldsymbol{v}2\pi rd\Omega + \int_\Omega \boldsymbol{T}\bullet(\nabla\boldsymbol{v})2\pi rd\Omega \\ &- \oint_\Gamma(\boldsymbol{T}\bullet\boldsymbol{v})\bullet\boldsymbol{n}2\pi rd\Gamma - \int_\Omega \boldsymbol{f}_r(\alpha)\bullet\boldsymbol{v}2\pi rd\Omega\end{aligned} \tag{A.1}$$

The first term of the right side of eq. (8), which corresponds to the convective term of the Navier-Stokes equations, can be further developed. First, it can be rewritten by reordering its terms and using the product rule for derivatives as

$$(\nabla\boldsymbol{v}\bullet\boldsymbol{v})\bullet\boldsymbol{v} = ((\boldsymbol{v}\bullet\nabla)\boldsymbol{v})\bullet\boldsymbol{v} = \frac{1}{2}(\boldsymbol{v}\bullet\nabla)(\boldsymbol{v}\bullet\boldsymbol{v}) \tag{A.2}$$

Since $\nabla\bullet(\boldsymbol{v}(\boldsymbol{v}\bullet\boldsymbol{v})) = (\boldsymbol{v}\bullet\nabla)(\boldsymbol{v}\bullet\boldsymbol{v}) + (\boldsymbol{v}\bullet\boldsymbol{v})\nabla\bullet\boldsymbol{v}$ and by assuming incompressible flow (from the continuity equation (eq. (1)), $\nabla\bullet\boldsymbol{v} = 0$), eq. (A.2) becomes

$$(\nabla\boldsymbol{v}\bullet\boldsymbol{v})\bullet\boldsymbol{v} = \frac{1}{2}(\boldsymbol{v}\bullet\nabla)(\boldsymbol{v}\bullet\boldsymbol{v}) = \frac{1}{2}\left(\nabla\bullet(\boldsymbol{v}(\boldsymbol{v}\bullet\boldsymbol{v}))\right) \tag{A.3}$$

When integrating eq. (A.3) over the computational domain ($2\pi rd\Omega$), multiplying by ρ (as in eq. (A.1)), and assuming ρ to be constant (incompressible fluid), Gauss's divergence theorem can be applied, resulting in

$$\begin{aligned}\int_\Omega \rho(\nabla\boldsymbol{v}\bullet\boldsymbol{v})\bullet\boldsymbol{v}2\pi rd\Omega = \int_\Omega \frac{\rho}{2}\left(\nabla\bullet(\boldsymbol{v}(\boldsymbol{v}\bullet\boldsymbol{v}))\right)2\pi rd\Omega = \\ \oint_\Gamma \frac{\rho}{2}\left[\boldsymbol{n}\bullet(\boldsymbol{v}(\boldsymbol{v}\bullet\boldsymbol{v}))\right]2\pi rd\Gamma\end{aligned} \tag{A.4}$$

The first stress tensor term of the right side of eq. (8) can be simplified by considering eq. (3) and $p\boldsymbol{I}\bullet\nabla\boldsymbol{v} = p\nabla\bullet\boldsymbol{v} = 0$ (from the continuity equation (eq. (1))),

$$\begin{aligned}\int_\Omega \boldsymbol{T}\bullet(\nabla\boldsymbol{v})2\pi rd\Omega = \int_\Omega \mu(\nabla\boldsymbol{v} + \nabla\boldsymbol{v}^T)\bullet(\nabla\boldsymbol{v})2\pi rd\Omega = \\ \int_\Omega \frac{1}{2}\mu(\nabla\boldsymbol{v} + \nabla\boldsymbol{v}^T)\bullet(\nabla\boldsymbol{v} + \nabla\boldsymbol{v}^T)2\pi rd\Omega\end{aligned} \tag{A.5}$$

The second stress tensor term of the right side of eq. (8) can be unfolded by substituting eq. (3) and using the relation $\boldsymbol{I}\bullet\boldsymbol{v} = \boldsymbol{v}$,

$$\begin{aligned}\oint_\Gamma(\boldsymbol{T}\bullet\boldsymbol{v})\bullet\boldsymbol{n}2\pi rd\Gamma = &\oint_\Gamma[(\mu(\nabla\boldsymbol{v} + \nabla\boldsymbol{v}^T))\bullet\boldsymbol{v}]\bullet\boldsymbol{n}2\pi rd\Gamma \\ &- \oint_\Gamma p\boldsymbol{v}\bullet\boldsymbol{n}2\pi rd\Gamma\end{aligned} \tag{A.6}$$

Since, in 2D swirl flow, $\boldsymbol{v}_{\text{abs}}\bullet\boldsymbol{n} = \boldsymbol{v}\bullet\boldsymbol{n}$ (i.e. $v_r n_r + v_z n_z$, due to considering a 2D mesh), the equation for the pressure head (eq. (25)) can be rewritten as follows,

$$\begin{aligned}H = &\frac{1}{Q}\left[\oint_\Gamma\left(\frac{p}{\rho g} + \frac{{v_{\text{abs}}}^2}{2g}\right)\boldsymbol{v}_{\text{abs}}\bullet\boldsymbol{n}2\pi rd\Gamma\right] = \\ &\frac{1}{Q}\left[\oint_\Gamma\left(\frac{p}{\rho g} + \frac{{v_{\text{abs}}}^2}{2g}\right)\boldsymbol{v}\bullet\boldsymbol{n}2\pi rd\Gamma\right] = \\ &\frac{1}{\rho gQ}\left[\oint_\Gamma\left(p\boldsymbol{v}\bullet\boldsymbol{n} + \frac{\rho}{2}\left[\boldsymbol{n}\bullet(\boldsymbol{v}(\boldsymbol{v}_{\text{abs}}\bullet\boldsymbol{v}_{\text{abs}}))\right]\right)2\pi rd\Gamma\right] = \\ &\frac{1}{\rho gQ}\left[\oint_\Gamma\left(p\boldsymbol{v}\bullet\boldsymbol{n} + \frac{\rho}{2}\left[\boldsymbol{n}\bullet(\boldsymbol{v}(\boldsymbol{v}\bullet\boldsymbol{v} + 2v_\theta\omega_0 r + (\omega_0 r)^2))\right]\right)2\pi rd\Gamma\right]\end{aligned} \tag{A.7}$$

From eq. (A.7), a "relative" pressure head can be defined as

$$\begin{aligned}H_{\text{rel}} = &\frac{1}{\rho gQ}\left[\oint_\Gamma\left(p\boldsymbol{v}\bullet\boldsymbol{n} + \frac{\rho}{2}\left[\boldsymbol{n}\bullet(\boldsymbol{v}(\boldsymbol{v}\bullet\boldsymbol{v}))\right]\right)2\pi rd\Gamma\right] = \\ &H - \frac{1}{\rho gQ}\left[\oint_\Gamma\left(\frac{\rho}{2}\left[\boldsymbol{n}\bullet(\boldsymbol{v}(2v_\theta\omega_0 r + (\omega_0 r)^2))\right]\right)2\pi rd\Gamma\right]\end{aligned} \tag{A.8}$$

As can be noticed, eq. (A.8) features some terms that are also shown in eqs. (A.4) and (A.6). By substituting eqs. (A.4), (A.5), (A.6), and (A.8) in eq. (A.1),

$$\begin{aligned}&\underbrace{\int_\Omega\left[\frac{1}{2}\mu(\nabla\boldsymbol{v} + \nabla\boldsymbol{v}^T)\bullet(\nabla\boldsymbol{v} + \nabla\boldsymbol{v}^T)\right]2\pi rd\Omega}_{\text{Relative energy dissipation (viscous effect)}} \\ &\underbrace{-\int_\Omega \boldsymbol{f}_r(\alpha)\bullet\boldsymbol{v}2\pi rd\Omega}_{\text{Relative energy dissipation (porous medium effect)}} \\ &\underbrace{+\int_\Omega(2\rho(\boldsymbol{\omega}\wedge\boldsymbol{v}) + \rho\boldsymbol{\omega}\wedge(\boldsymbol{\omega}\wedge\boldsymbol{r}))\bullet\boldsymbol{v}2\pi rd\Omega}_{\text{Relative energy dissipation (inertial effects)}} = \\ &\underbrace{\oint_\Gamma[(\mu(\nabla\boldsymbol{v} + \nabla\boldsymbol{v}^T))\bullet\boldsymbol{v}]\bullet\boldsymbol{n}2\pi rd\Gamma}_{\text{Viscous stress effect}} - \underbrace{\rho gQH_{\text{rel}}}_{\text{Relative pressure head effect}}\end{aligned} \tag{A.9}$$

Therefore, the minimization of the relative energy dissipation given in eq. (15) is related to the maximization of the relative pressure head (H_{rel}) and, therefore, to the (absolute) pressure head (H). Borrvall and Petersson [14] neglect the "Viscous stress effect" of the right side of eq.

(A.9), in order to show the relation of the energy dissipation to the variation of pressure weighted by the flow rate (i.e., the static pressure term of the pressure head), and also does not include the convective term, which is the non-linear Navier-Stokes term not present in the Stokes equations.